

Muon Piston Calorimeter Calibration

Mickey Chiu^a, Matthias Große Perdekamp^b, John Koster^c, Beau Meredith^b, Scott
Wolin^b

^a Brookhaven National Laboratory

^b University of Illinois at Urbana Champaign

^c RIKEN BNL Research Center

Abstract

In this note we document the Muon Piston Calorimeter (MPC) calibration procedure used on the 2008 dataset. This is the first time the complete detector took data for an extended period of time and a similar procedure is expected to be used on subsequent datasets.

The energy resolution is estimated to have a 4% constant term and 80 MeV noise term. The global energy uncertainty is 2%.

Contents

1 Overview	2
2 FEM calibration	3
2.1 Pedestals	4
2.2 High to low gain conversion factors	4
2.3 ADC and TDC overflow determination	5
3 Absolute energy scale: Part I	5
3.1 Description	5
3.2 Minimum ionizing particle peaks	6
3.3 Inverse slopes	8
4 Relative gain changes	10
4.1 Description	10
4.2 Implementation	12
5 Absolute Energy Scale: Part II	13
5.1 Procedure	13
5.2 Results	14
6 π^0 and η two-photon peaks	24
6.1 Minimum reconstructible mass	24
6.2 Energy and mass resolution	24
6.3 Identification of mis-calibrated towers	26
6.4 π^0 and η identification	28
6.5 Fractional mass resolutions from data	28
6.6 Gain stability	32
6.7 Comparison to Monte-Carlo	32
A Confirmation of Channel Mapping	40
B $M_{\gamma\gamma}$ distributions binned in E_{pair} with η fit	40
C $M_{\gamma\gamma}$ distributions binned in $p_{T,pair}$ with η fit	48
D $M_{\gamma\gamma}$ distributions binned in E_{pair} with π^0 fit	53
E $M_{\gamma\gamma}$ distributions binned in $p_{T,pair}$ with π^0 fit	60

1 Overview

The South MPC was first installed for the 2006 run, then the North MPC was added for the 2007 run. For the 2007/2008 run both detectors received an improved LED gain monitoring system. From that point and on, the MPC should be relatively stable in terms of its composition. Therefore, we are writing this note to document the first calibration done on the MPC in its mature form.

For each event and each tower, the uncalibrated energy is converted to energy as:

$$E_i = G_i \cdot R_i(t) \cdot ADC_i \quad (1)$$

where:

- i stands for a given tower.
- E is the calibrated energy deposited in a tower
- G_i is the tower's absolute gain defined for one reference run
- $R_i(t)$ is a relative gain between a reference run and all other times. The smallest interval in time we use in the MPC is one run.
- ADC_i is defined as:

$$ADC = ADC_{post} - ADC_{pre} - (ADC_{post,pedestal} - ADC_{pre,pedestal}) \quad (2)$$

The determination and confirmation of these factors are elaborated upon in this note and summarized in figure 1. An important point to remember is that while the MPC shares many similarities to the central arm, its location is very different. Experience and assumptions from the central arm may not transfer well to the forward region. For example: Energy $\neq p_T$, and energy $\neq C p_T$ where C is a global scale. The true relation is: energy = $C(\eta) p_T$. $C(\eta)$ changes by roughly a factor of 3 between the inner and outer edges of the detector. The calibration consists of four main pieces:

1. FEM Calibrations deal with preparing the best possible raw ADC values. These are fairly standard in PHENIX and well-known from the Central Arm Calorimeter.
2. Determining the absolute energy scale (G_i), which we do tower-by-tower and fill-by-fill using minimum ionizing particle peaks. The statistical uncertainty for each tower and fill is $\sim 10\%$. If the MIP fits fail, the gain is estimated using an inverse slope method. This calibration is further refined using an iterative π^0 peak position procedure. However, the run-to-run relative gain changes are also used in this method.
3. $R_i(t)$ is measured using an LED-based monitoring system. In contrast to the MIP calibration, the statistical uncertainty for a given tower and run is approximately 2%.

4. Confirmation of the absolute and relative calibrations is done in three steps using the physics observables: clusters and pairs of clusters.
 - (a) Identify mis-calibrated towers (warnmap): we generate a list of badly calibrated towers based on a plot of the number of tower hits versus the tower radial distance from the beampipe, and used an LTS regression fit to find outliers.
 - (b) Detector stability: We fit $M_{\gamma\gamma}$ peaks to extract the π^0 and η peak positions as a function of time, and check that they are constant.
 - (c) We compare the π^0 and η peak properties to Monte-Carlo.

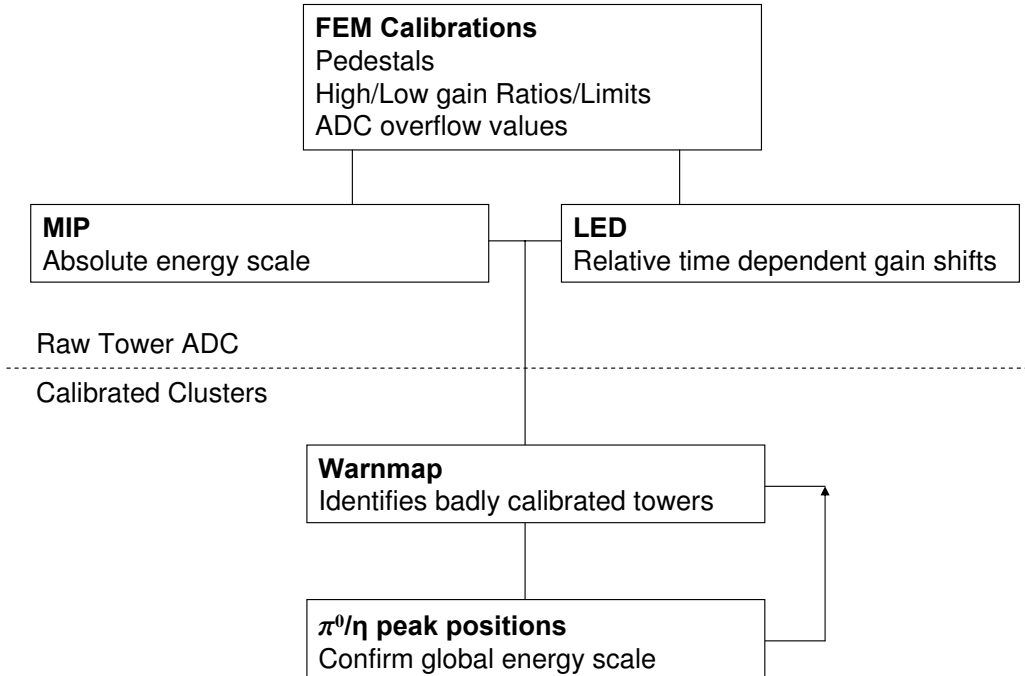


Figure 1: Outline of the calibration procedure.

2 FEM calibration

The FEM calibration consists of three steps:

- Pedestals

- High to low gain conversion factors
- ADC and TDC overflow determination

2.1 Pedestals

The pedestals are stable over the course of an entire run (e.g. run08). They are found from collecting data while the detector is ready for physics data but there is no beam in the ring, and with a noise trigger.

2.2 High to low gain conversion factors

Two ADC values are available for a given tower and event. The first is called low gain ADC and the second high gain ADC. The conversion from high to low gain is done with a simple scaling formula:

$$ADC_{low,i} = C_i \cdot ADC_{high,i} \quad (3)$$

where ADC is defined in equation 2, C_i is a constant conversion factor which depends on the tower, i. Determining C_i is first goal of the calibration. The second goal is to determine the end point of the dynamic range of the high gain ADC. Both parameters are illustrated in figure 2. The high to low gain conversion factors are found by generating

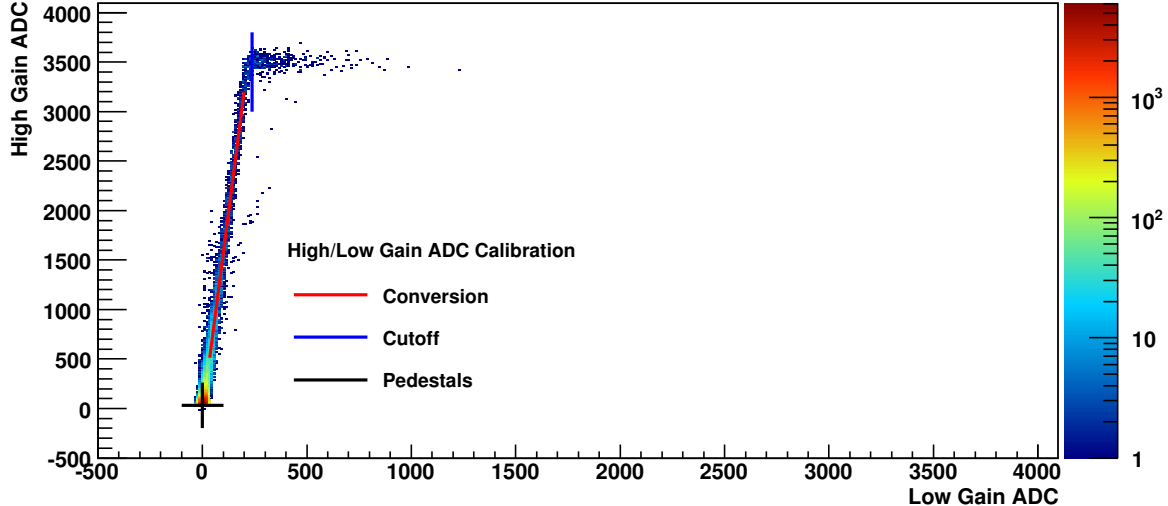


Figure 2: High to low gain correlation plot. Line overlays correspond to the pedestals (black) which have already been subtracted, the conversion between high and low gain (red) and the high gain cutoff value (blue).

a correlation plot between the high gain ADC and the low gain ADC. The high to low gain conversion is found by fitting the correlation plot between 0 and the high gain cutoff value with a straight line. The line's slope is the conversion factor. The expected value is ~ 16 .

2.3 ADC and TDC overflow determination

The last calibration determines the low gain ADC overflow value and the TDC timeout value. For the 2008 data collection period they are determined in different ways, but the goal is the same: determine the point at which a histogram's counts spike at high values. We go into some detail on the TDC overflow values, but a similar procedure is used to find the ADC overflows. First, we generate tower-by-tower histograms of the TDC's from the central tower of each cluster. We run on MPC triggered and Minimum bias triggered data separately. For each tower's histogram we then iterate over each bin with bin center greater than 2000. If the bin content exceeds 1% of the total histogram population the bin is a candidate. We then integrate the histogram contents several bins beyond the candidate to the end of the histogram. If counts stay below 10% of the total histogram's population, then we accept the candidate as the TDC overflow value. Figure 3 shows an example output plot from the procedure. The tower-by-tower TDC

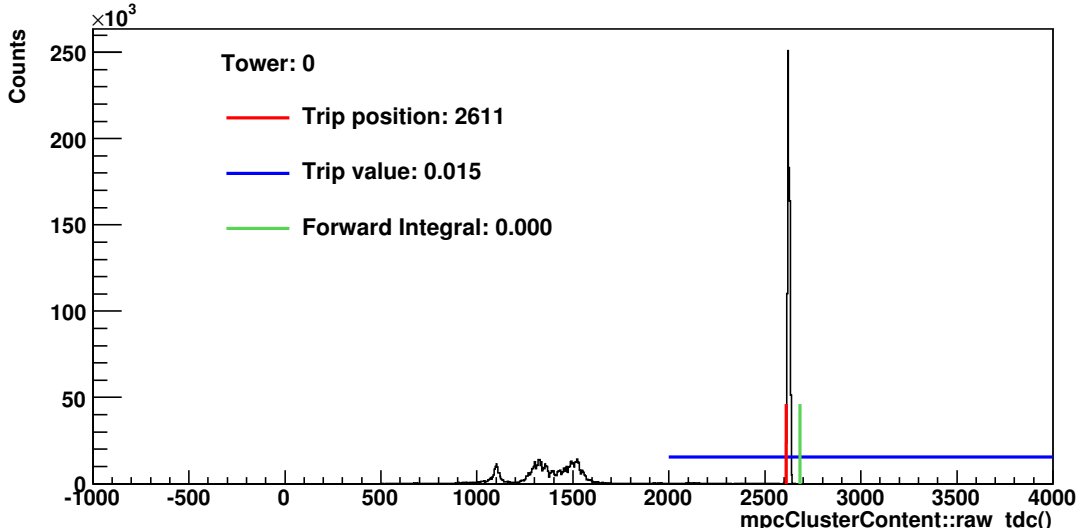


Figure 3: Tower 0, Trigger: MPC, TDC spectra from mpcClusterContent's of disk-resident run08 files. Line overlays correspond to the algorithms chosen timeout value (red), 1% threshold point (blue) and start point for the forward integral (green)

spectra for MPC-triggered data along are provided for inspection in [6]. The values are summarized in figure 4.

3 Absolute energy scale: Part I

3.1 Description

The absolute energy scale is determined by finding the position of minimum ionizing particle peaks. The position is expected at 234 MeV. The method was originally developed for the two day $\sqrt{s} = 62\text{GeV}$ $p^\uparrow p$ in 2006[1]. The method was further refined for run08

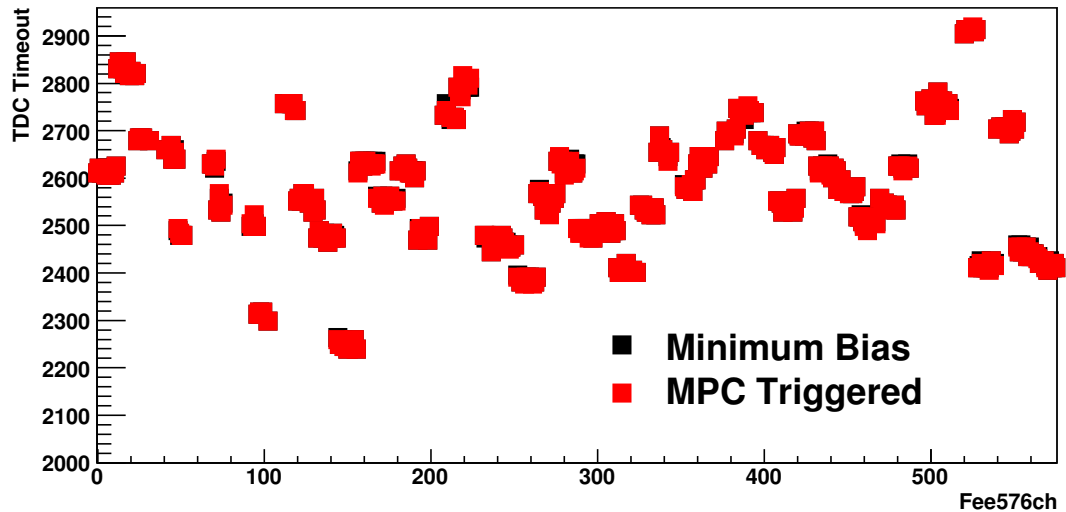


Figure 4: TDC timeout points (Y-axis) drawn for each tower (X-axis). South towers are below 288, North towers above. The values are shown to agree between the minimum bias and MPC triggered datasets.

but its essential elements remain unchanged. If we fail to extract a peak position, we use an inverse slope method to determine a tower's gain. The absolute energy scale is further refined using an iterative π^0 peak position procedure. This procedure is similar to the one used in the central arm.

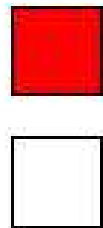
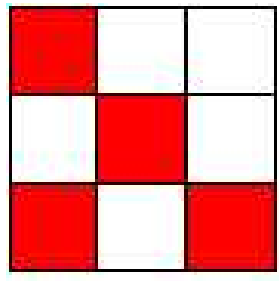
3.2 Minimum ionizing particle peaks

The peaks are extracted by generating a histograms of high gain ADC for each tower and each fill with different cuts designed to enhance the yield of charged tracks applied to each histogram. The two variables which are cut against are:

1. High energy bit sum – number of active towers surrounding a given tower. Maximum is nine. Electromagnetic showers are expected to have a high bit sum while MIP's should have low bit sums. Overlapping cuts are implemented as: $\text{bitsum} \leq \{2,3,4\}$. See figure 1 for an illustration. The definition of a “hit” MPC tower is greater than zero counts high gain ADC value.
2. dR – distance from the nearest active BBC tube to a track from the MPC tower to the collision point. An active BBC tube is defined as a tube with both its TDC values less than 2700 counts. Overlapping cuts are implemented as: $dR \leq \{2,3,4,5\}$ cm. See figure 2 for an illustration.

The code is available here:

```
offline/packages/mpc/online/MpcMip.{C,h}
```



Active MPC Tower
Inactive MPC Tower

Figure 5: Illustration of the high energy bitsum. The bitsum for the central tower is 4

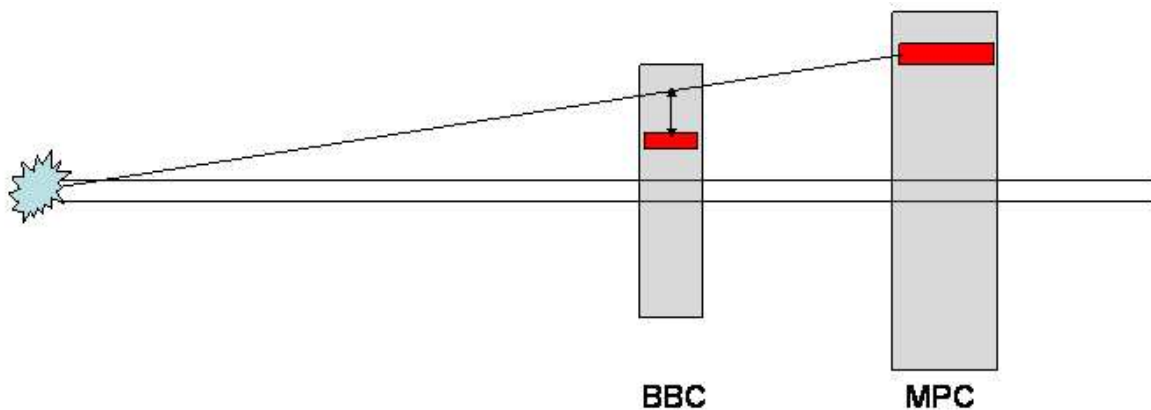


Figure 6: Illustration of the dR variable.

The grid is searched from most selective to least selective cut for a good MIP peak fit, and the search is stopped as soon as one is found. The fit function is a power law plus a Gaussian. Good fits are defined using a variety of criteria:

1. Number of counts > 100
2. $\chi^2 < 300$
3. Gaussian amplitude > 0
4. $11 < \text{Gaussian center} < 40$
5. Gaussian width < 11

The number of MPC towers is only 416, so visual inspection of the fitting is also done and in some cases the definition of a good fit is adjusted. An example peak is shown in figure 7

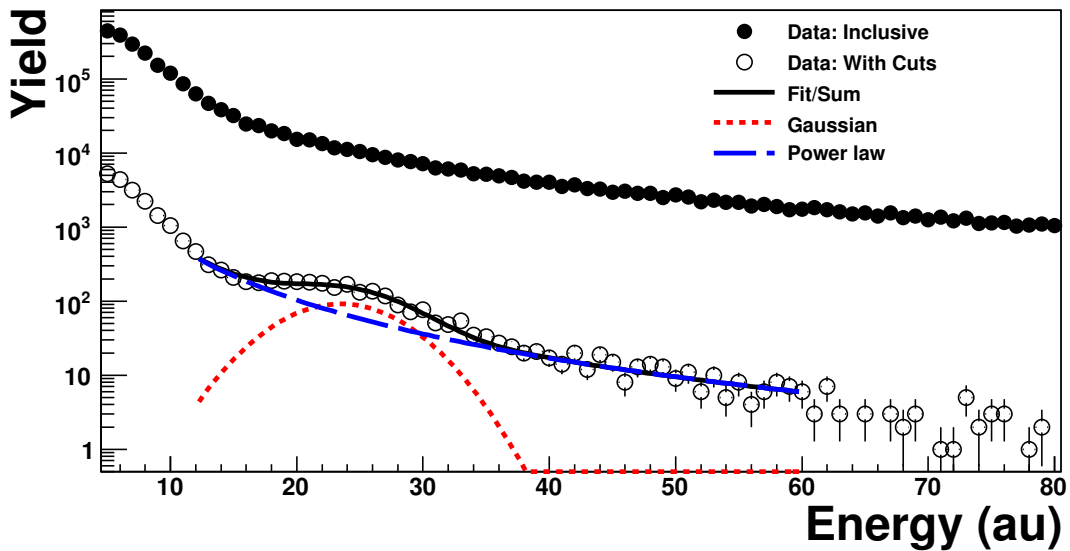


Figure 7: Example MIP peak from tower 270 and fill 9919. The filled points are the inclusive spectrum and the open points are with coincidence cuts with the BBC tubes and bitsum cuts.

3.3 Inverse slopes

In cases where the MIP fit fails to determine a gain for a particular tower, we use the inverse slope method. Here we use the fact that the high energy spectrum of a tower goes like:

$$f(E_{\text{tower}}) = kE_{\text{tower}}^{-a} \quad (4)$$

where k and a are constants which depend on the specific tower. By looking at the normalized distribution, we can reduce the number of independent variables to one. If we insert equation 1 (but ignore the time dependent factor) and take the log of both sides we get:

$$\log(f(E)) = \log(k \cdot G_i^{-a}) - a \cdot \log(ADC_i) \quad (5)$$

Therefore, we can extract the tower by tower gains (G_i) by taking the log intercept from a power law fit to the tail of raw ADC spectrum (with no *bitsum* or *dR* cuts) from the minimum bias dataset. An example fit is shown in figure 8.

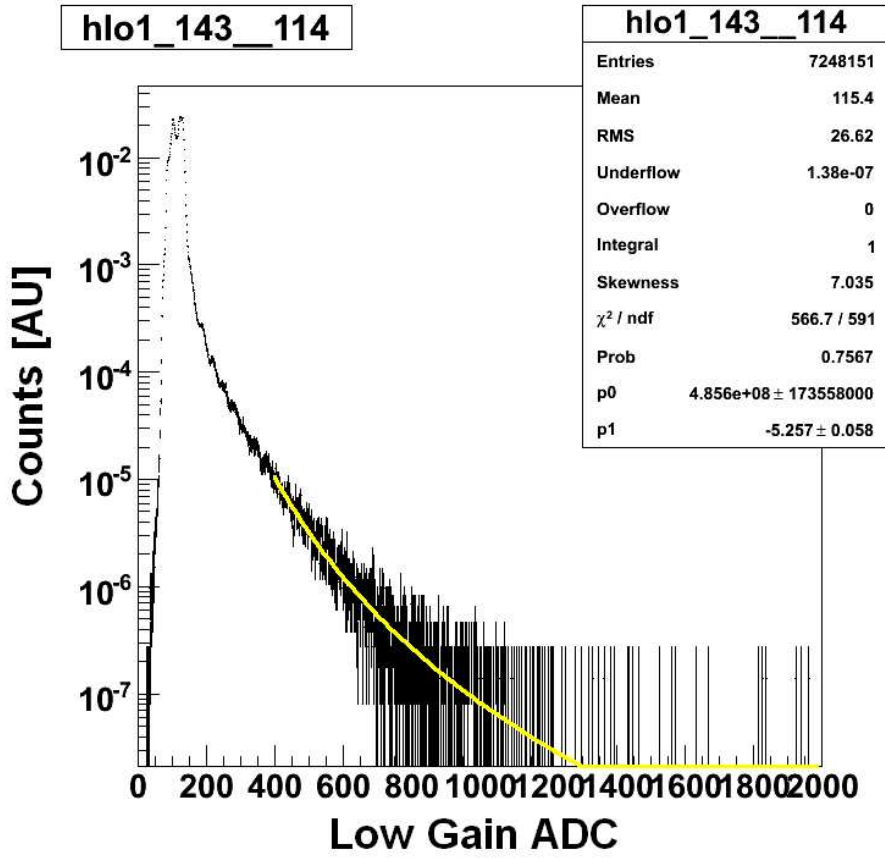


Figure 8: Example log intercept fit from tower 143.

It is important to note that we can not extract an absolute energy scale using log intercept, because although we can extract the a gain, we have no baseline energy to work with. To get an absolute scale, we look at the expected correlation between the log intercept and MIP for towers where we found a MIP. To find the absolute energy scale for towers with only a log intercept parameter and no MIP peak, we use the correlation plot shown in figure 9. The combined MIP and log intercept energy calibration results are inserted in the database for analyzers to use.

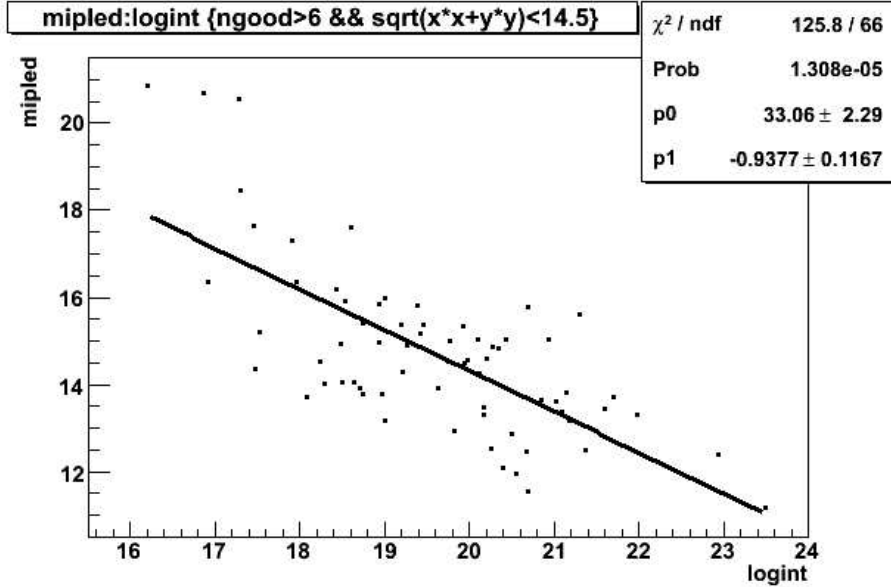


Figure 9: Correlation between the inverse slope parameter and the minimum ionizing particle peak position. Each point corresponds to a single tower's inverse slope and MIP position averaged over all of run8.

4 Relative gain changes

4.1 Description

There are two major effects which cause the gain to change with time. The first is temperature. During steady-state running the temperature is essentially constant, but when the current in the muon magnets are shut off (i.e. for an access day) the temperature of the muon magnets and the MPC drop rapidly. After the magnets are turned back on, the whole apparatus warms up over a period of days to weeks. Both the light-yield of the PbW₀₄ crystals and gain of the avalanche photo-diodes (APD) varies with temperature. In the case of the APD it has been measured to cause a -2%/° Celsius change in the gain[2]. The second major time-dependent effect is an apparent effect from radiation damage. The LED signals from the MPC go down with time into a run. However, once the run is over the LED signals gradually return to their previous values. Both effects are shown in figure 10. For the full details of the MPC monitoring system please read its dedicated technical note [2]. The LED system appears to track the MPC gain quite well; applying an LED-based gain correction removes time dependent shifts in the π^0 and η peak positions. However, the LED system should not in general be trusted blindly. The MPC LED system injects light at one end of the crystal and is collected at the other end using an APD. Therefore:

1. The light-yield of the crystal is not probed. Any effects related to loss of light yield over time cannot be detected by an LED-based system. Potential effects are temperature and radiation damage.

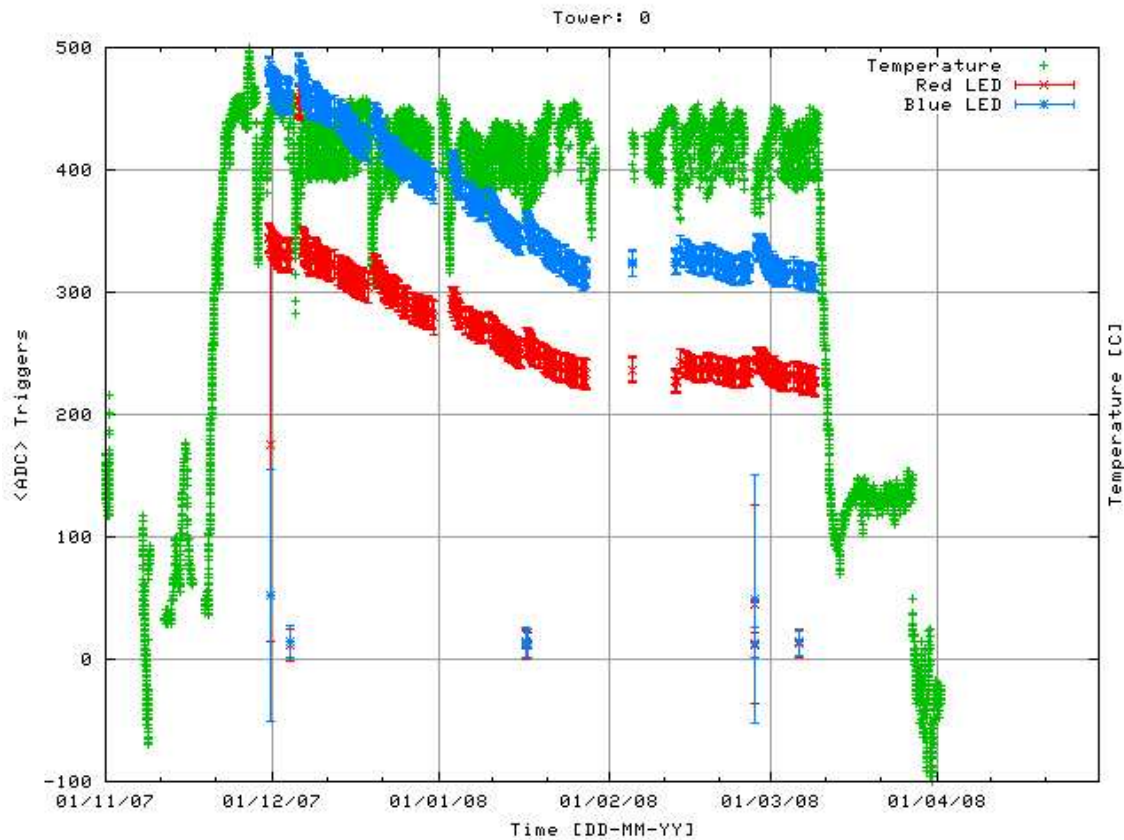


Figure 10: The raw ADC values for tower 0 for red and blue led light shown in red and blue and the temperature of the MPC (green) plotted against time. The full-scale time window is all of run8 (dA+pp). There is a large drop in gain over the run which suggests radiation damage and also spikes in increased gain caused by temperature drops in the muon magnet system. The muon magnet currents aren't shown on the plot, but the periods of decreased temperature correspond to access days.

2. The LED light propagates the entire length of the crystal while the scintillation light from electromagnetic showers is generated randomly and in an energy-dependent way continuously throughout the crystal.

For all periods of data-taking, an LED system flashes the towers a rate of 2 Hz. For each run and each tower, a histogram is generated of the low gain ADC. An example plot is shown in figure 11. The LED value for an individual tower and an individual run is taken as the mean of the distribution. By itself this value is meaningless, but comparing this value between runs gives access to how the gain changed with time.

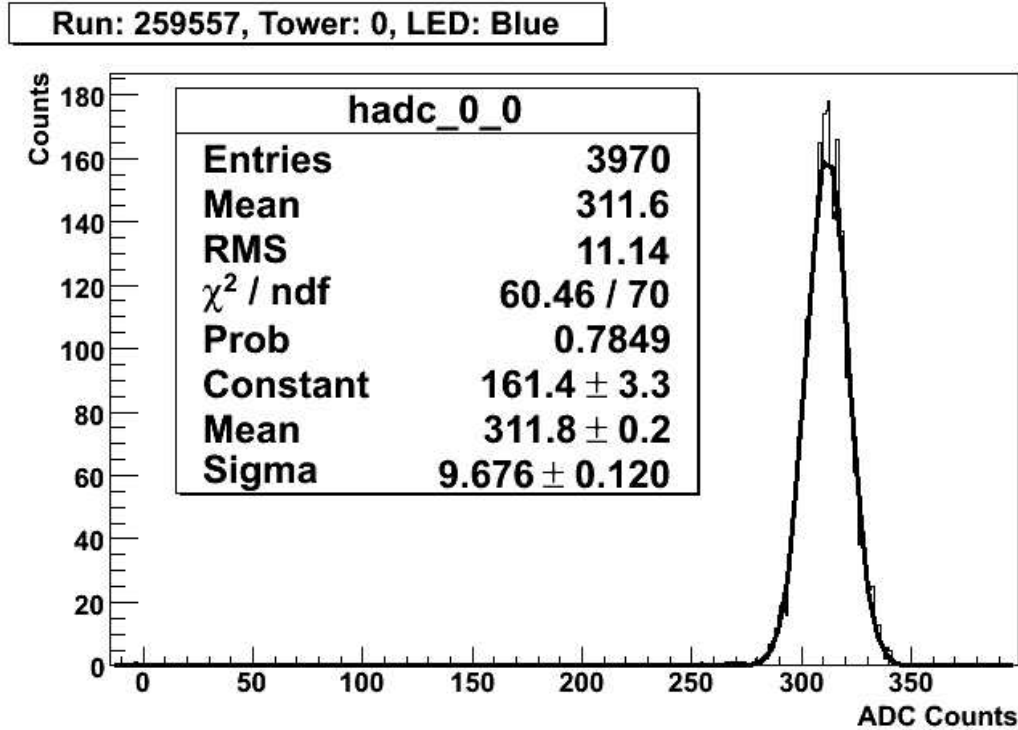


Figure 11: Yaxis: Counts, Xaxis: ADC from LED-triggered events from runnumber 259557 and tower 0.

4.2 Implementation

The MPC led code is implemented in the online calibration system and the code can be found here:

<online/calibration/onlcal/subsystems/mpc/>

Histograms and text files are automatically generated through the OnlCal system. In addition, the results of the calibration are automatically stored in the calibrations database. The stability of the detector within a given run is checked by calculating sub-run averages of the ADC and calculating the χ^2/NDF value of the sub-run means to the mean over the entire run. The detector is shown to be stable within a run. The results are separated by

red or blue LED light, and by whether the raw ADC is stored or the ratio of the tower ADC and reference pin diode ADC. The results are separated from one another by the “bank id”. None of the original four values are used in analysis. Instead, a smoothing macro defines a master run (e.g. 259252), and passes over the an entire run’s (e.g. run8) worth of data outputting a smoothed gain relative to the reference run. This smoothed and relative value is entered into the database using a new bank id, and is used as a scale factor to a particular snapshot in time.

5 Absolute Energy Scale: Part II

This section describes the iterative π^0 procedure which is used to further refine the energy calibrations described in section 3. The iterative calibration tries to match the mass of the π^0 in each tower to a mass determined by simulation. For simulation, we run Pythia $\sqrt{200}$ GeV p+p collisions through GEANT and reconstruct the π^0 mass in each tower (A histogram with the two-cluster invariant mass distribution is formed for each tower. Entries into the histogram are made when a tower is the central tower of a cluster (highest energy). Hence, for each cluster pair, there is an entry for two different towers). The simulation has been tuned to match the electronics noise and the stochastic fluctuations with those in the data. The Pythia simulations (Tune A) have been shown to match the per-event yield of π^0 s quite well. A list of simulated masses for each tower are given in

```
offline/packages/mpc/calibrations/pi0cal_fast/macros/iterative/sim_means_combined.txt
```

The MPC stores ADC values rather than cluster energies (as in the EMCal), so in principle it is possible to perform the iterative calibration with re-clustering for every iteration. However, it is much quicker to use a simplifying assumption that the position of the cluster does not change upon modifying the energies in the cluster, and only the tower energies in the cluster do change. One has to essentially perform the calculation of ecore from the tower energies in mpcClusterContent, but this takes very little time relative to reclustering. Upon using these assumptions, calibration of the detector takes much less than a day. One should note that without the LED’s to track the time-dependence, this procedure would be much more difficult.

5.1 Procedure

First we write out a TTree with cluster pairs passing some minimal set of cuts. This class and macros are available at

```
offline/packages/mpc/calibrations/pi0cal_fast/mpcPi0TTree
offline/packages/mpc/calibrations/pi0cal_fast/macros/data
```

Then, the TTree output from the last step is fed into the macro

```
offline/packages/mpc/calibrations/pi0cal_fast/macros/iterative/ana_pi0cal.C
```

This macro takes output from the Subsysreco class mpcPi0TTree and uses it to improve the calibrations for the MPC. The idea is to match the π^0 mass value in each tower to that determined from running 200 GeV p+p Pythia through GEANT. The value of the mass is changed by taking

$$gain_{new} = gain_{old} \times m_{sim}/m_{reco} \quad (6)$$

Nominally speaking, $m_{sim} = 0.135\ GeV/c^2$; however, we tried to best match the response of the detector by using the simulated masses.

A simplified procedure was used to find the value of the mass in each bin. There is no subtraction, but rather a Gaussian is fit a small region ($\pm 25\ MeV$) around the maximum of the mass peak. The mean value and standard deviation are then calculated from this fit; the standard deviation is still a good measure of the width of the peak, but is not an exact measure.

The procedure used has many of the tools used in reconstruction, and hence if the cluster reconstructoin changes then this code must be changed accordingly. These include the x, y shifts from center of gravity coordinates to actual hit positions, calculating E_{core} , and using the shower shape.

Eight iterations are performed to get the procedure to converge. The cuts made (some are made in mpcPi0TTree) are:

- $fabs(zvtx) < 30.0\ cm$
- $E_{clus} > 2\ GeV$
- $\chi^2/NDF < 3$
- $Max(disp_x, disp_y) < 4.0$
- $p_{T,pair} > 0.45\ GeV/c$
- $9\ GeV < E_{pair} < 17\ GeV$
- $E_{asymm} < 0.6$

5.2 Results

Results from a few of the iterations are shown in Figs. 12-15, and the gain changes are shown in Fig. 16. Additionally, the invariant mass peaks of all towers are shown for the first and last iteration in Figs. 17-20.

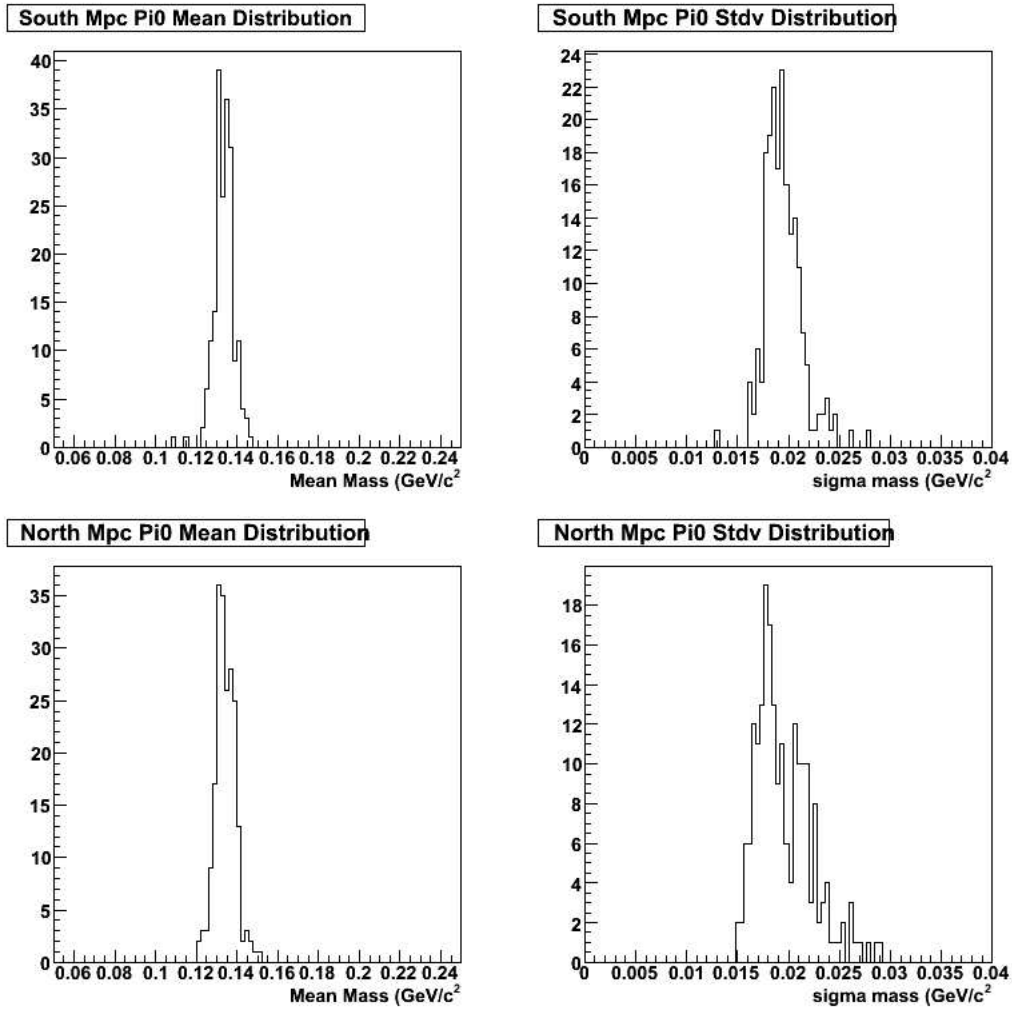


Figure 12: Mass and Stdv of north, south MPC before 1st iteration of the pi0cal

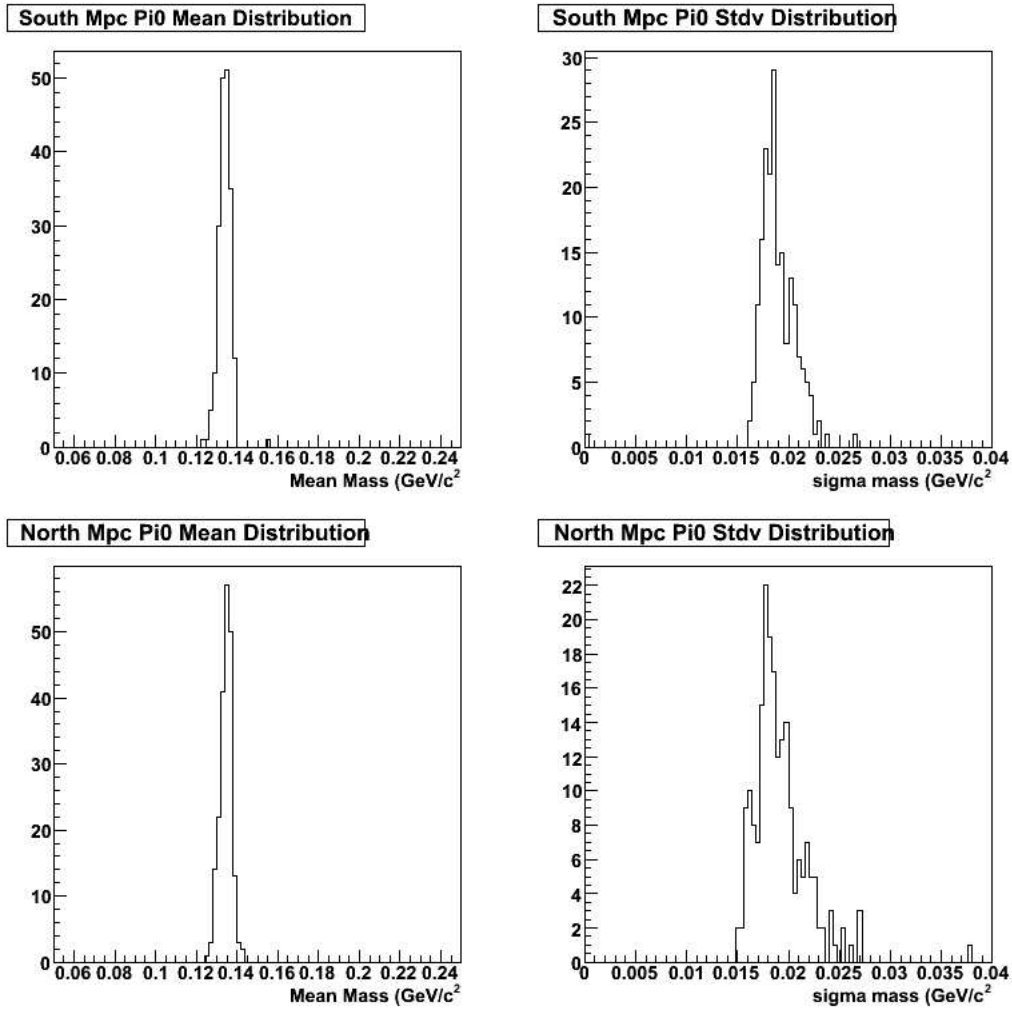


Figure 13: Mass and Stdv of north, south MPC before 3rd iteration of the pi0cal

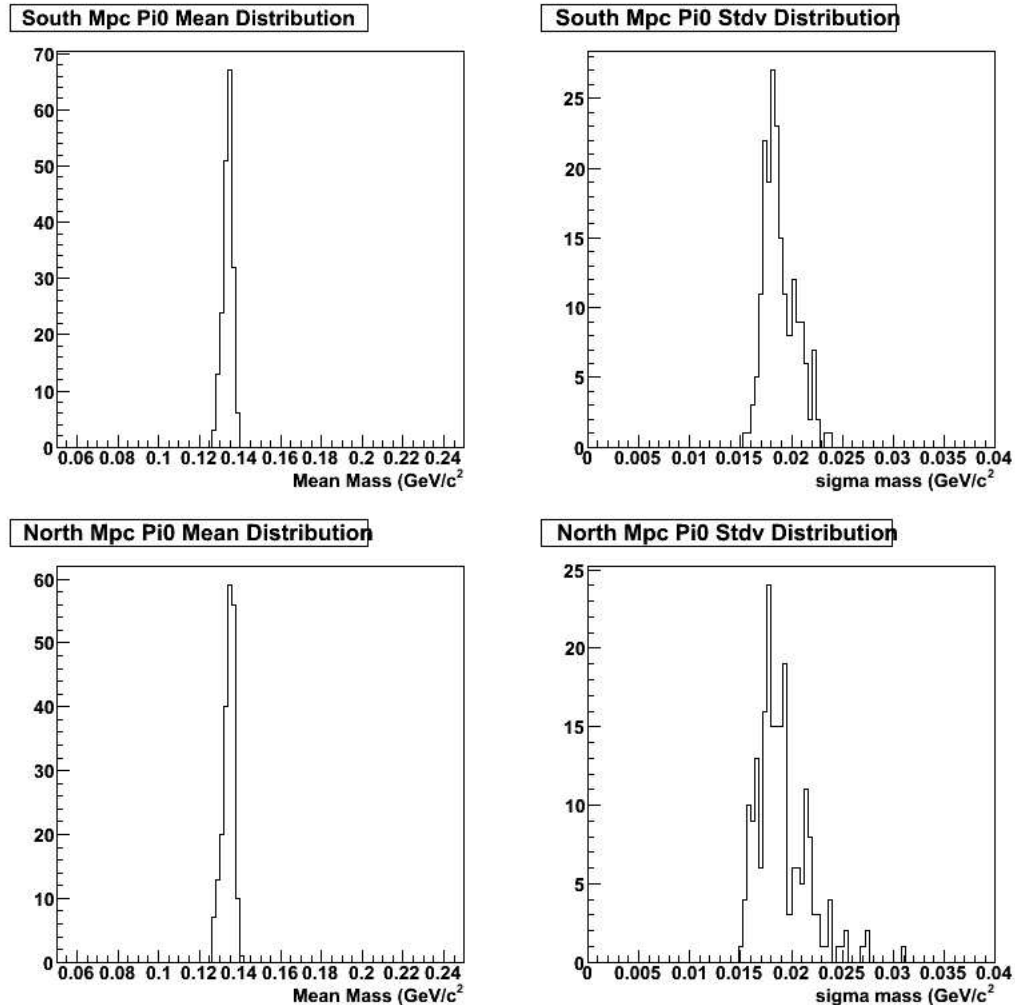


Figure 14: Mass and Stdv of north, south MPC before 5th iteration of the pi0cal

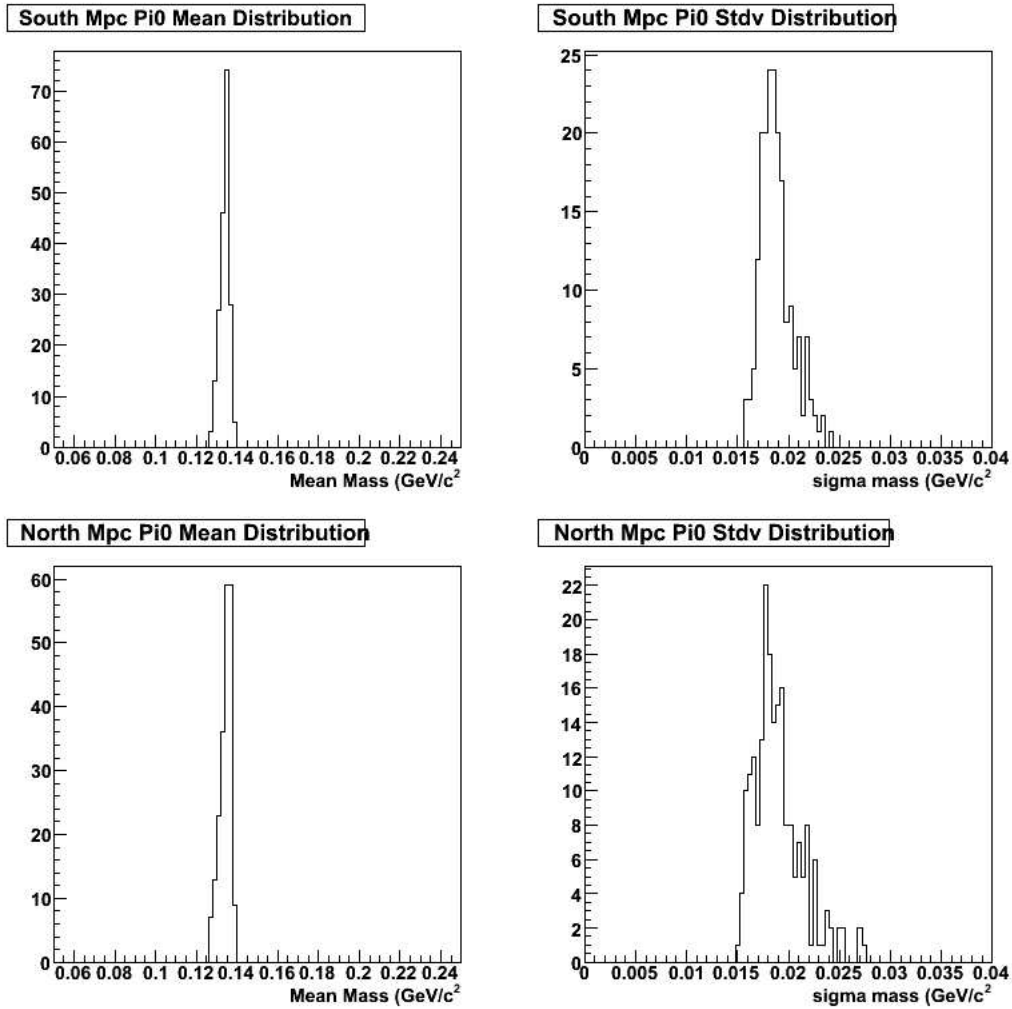


Figure 15: Mass and Stdv of north, south MPC before 7th iteration of the pi0cal

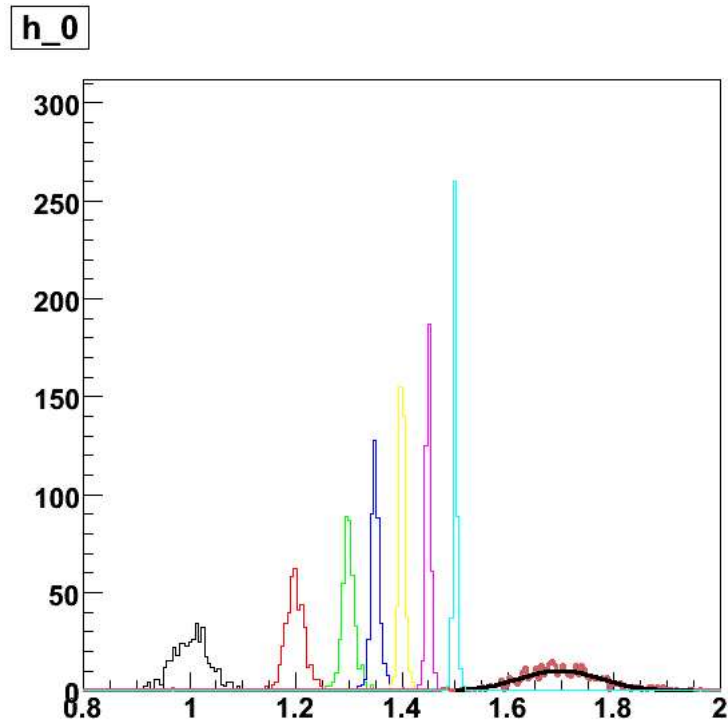


Figure 16: This illustrates the changes in each iteration. Each peak represents that changes in the gains from the previous iteration. The last peak represents the total change in the gains throughout the whole process.

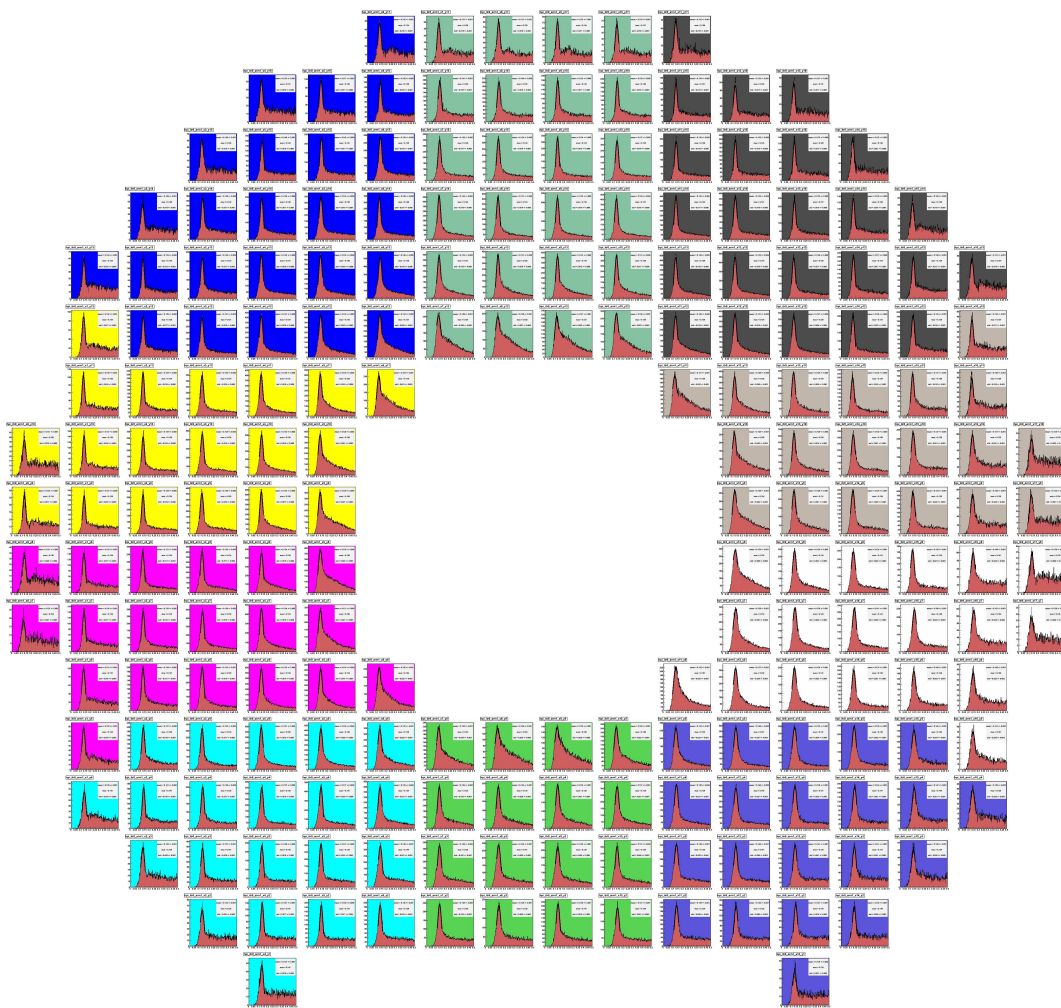


Figure 17: Masses before from MIP + LED in north MPC

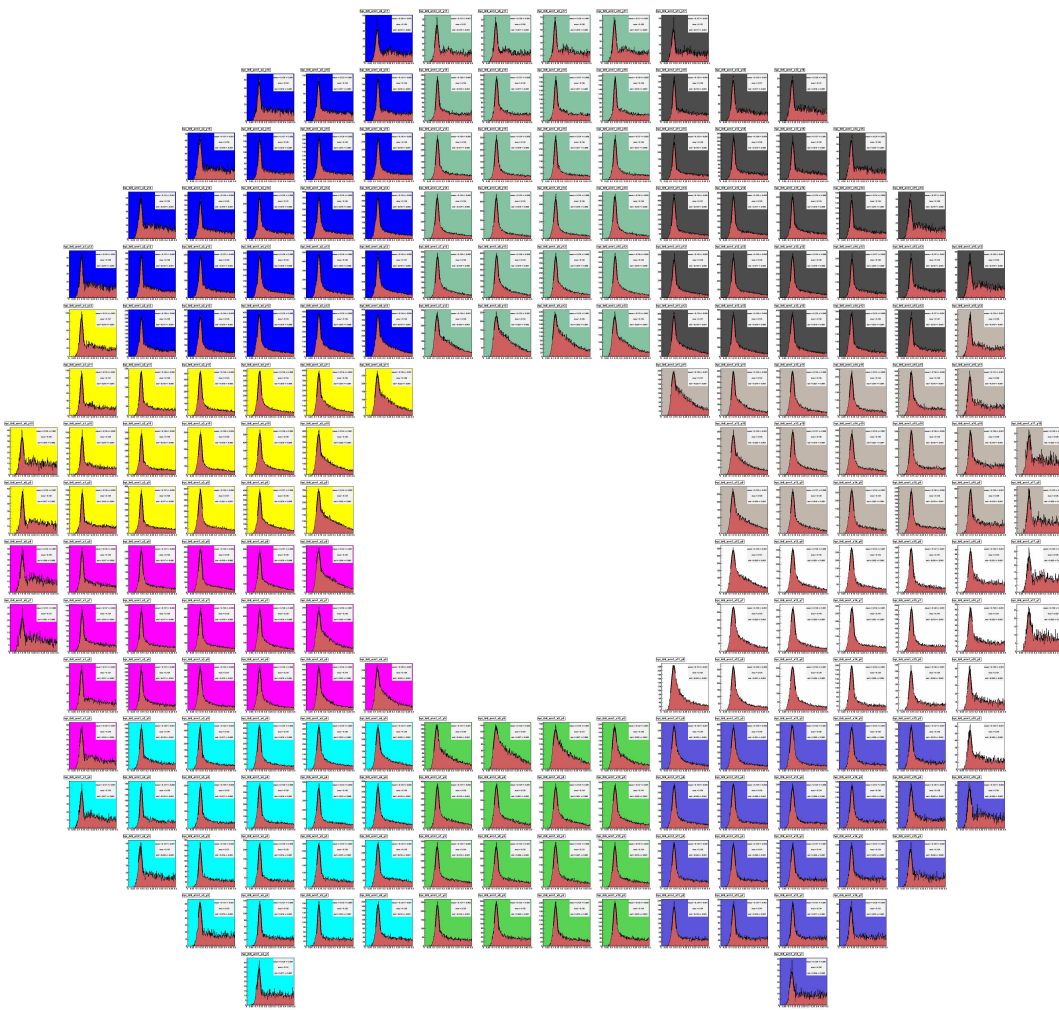


Figure 18: Masses after pi0cal in north MPC

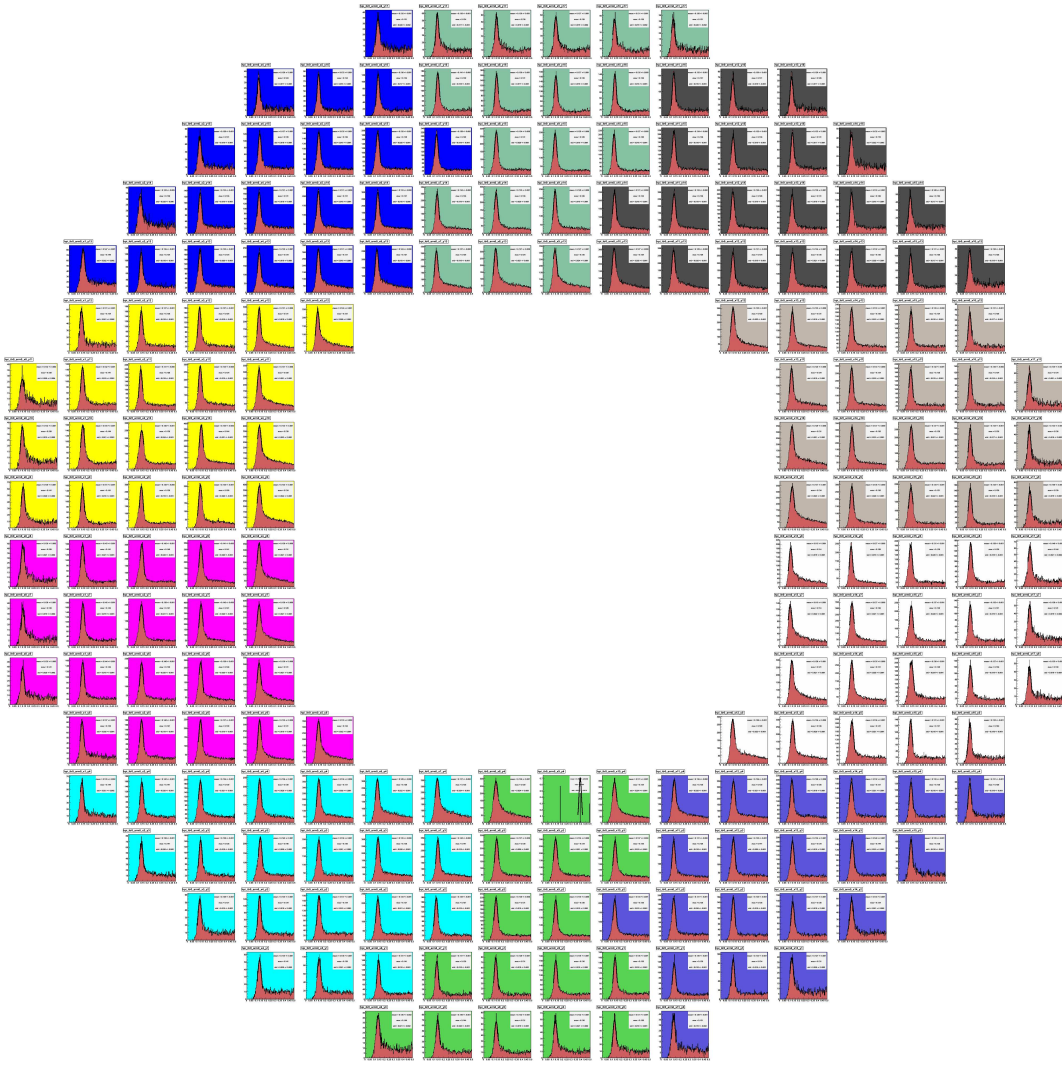


Figure 19: Masses before from MIP + LED in south MPC

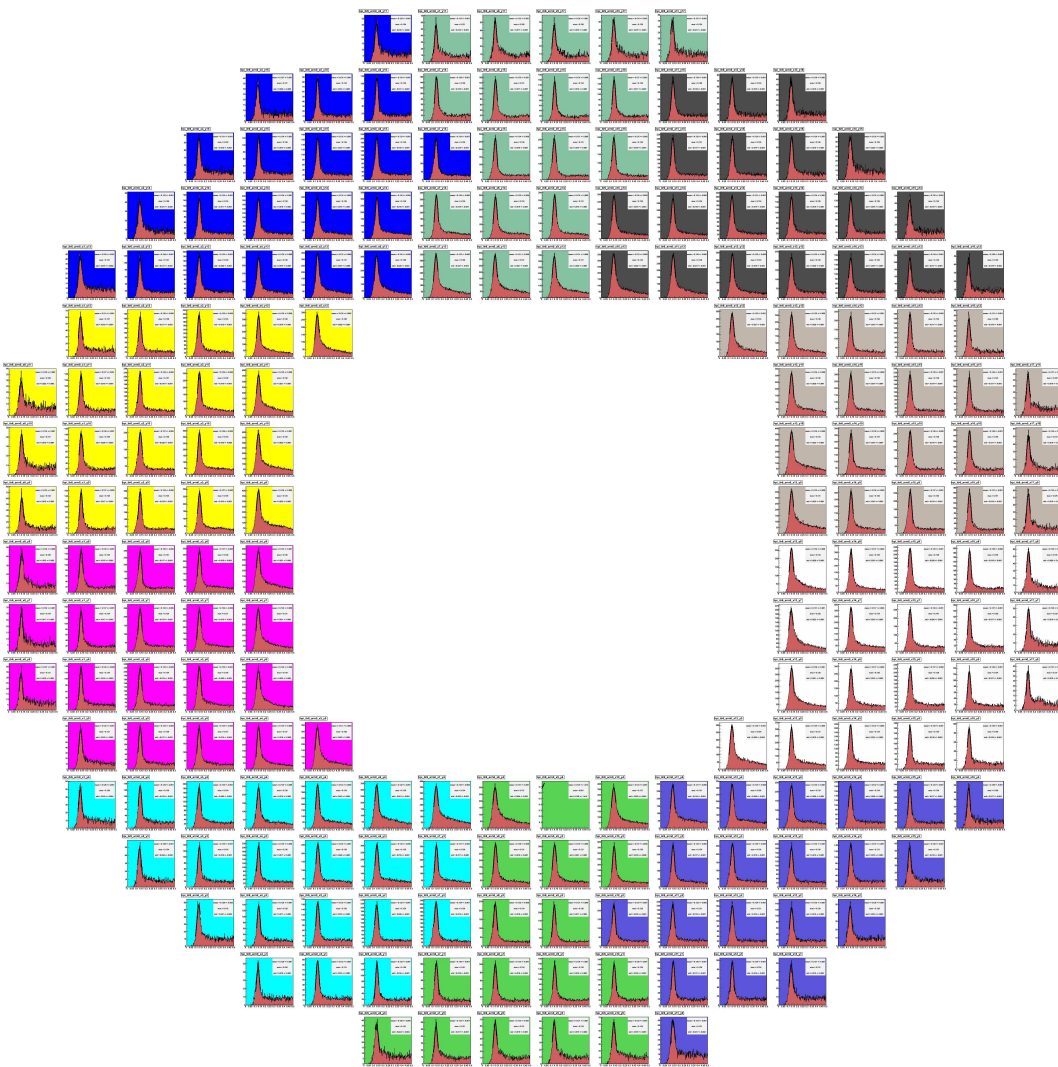


Figure 20: Masses after `pi0cal` in south MPC

6 π^0 and η two-photon peaks

This section's goal is to: discuss the general π^0 and η reconstruction performance of the MPC, the procedure used to identify badly calibrated towers and then compare the properties of the peaks to simulation.

6.1 Minimum reconstructible mass

The clustering algorithm has a minimum cluster separation distance beyond which it cannot separate clusters. This distance is approximately 2.6 cm (the tower size is 2.2 cm). This minimum cluster separation sets a minimum opening angle on the cluster pairs, and therefore an energy dependent minimum reconstructible mass according to the formula:

$$m_{\gamma\gamma}^2 = 2E_1E_2(1 - \cos(\theta)) \quad (7)$$

where θ is the opening angle between the clusters, and $E_{1,2}$ refer to the energies of the arbitrarily ordered clusters. The expression can be written in terms of the pair energy E_{pair}

$$m_{\gamma\gamma}^2 = \frac{1}{2}E_{pair}^2(1 - \gamma^2)(1 - \cos(\theta)) \quad (8)$$

where the energy asymmetry between the photons, γ is defined as:

$$\gamma = \left| \frac{E_1 - E_2}{E_1 + E_2} \right| \quad (9)$$

After inserting the minimum reconstructible opening angle corresponding to 2.6 cm, an energy asymmetry of 0.6 (maximum allowed γ in a typical analysis) and a pair energy of 15 GeV, the resulting minimum mass is 71 MeV. See figure 21 for a plot of the minimum mass plotted against energy. This effect reduces counts at the low mass side of the $M_{\gamma\gamma}$ distribution in an energy dependent way, and leads to a π^0 peak position which shifts up as a function of pair energy. Despite this hard-cutoff at low mass, the peak retains a Gaussian-like shape due to detector resolution effects and the fact that the vertex distribution is quite broad. Collisions either nearer or farther away from the detector shifts the minimum reconstructible mass to either larger or smaller values than the ones shown in figure 21.

6.2 Energy and mass resolution

The energy resolution of a calorimeter is typically parameterized as:

$$\frac{\sigma(E)}{E} = \frac{a}{\sqrt{E}} \oplus \frac{b}{E} \oplus c \quad (10)$$

where the three terms: a, b, c are called: stochastic, noise and constant. For an extended discussion of each term please see reference [5]. It is important to note that the energy and mass fractional resolutions are not the same. If we assume that the energy resolution

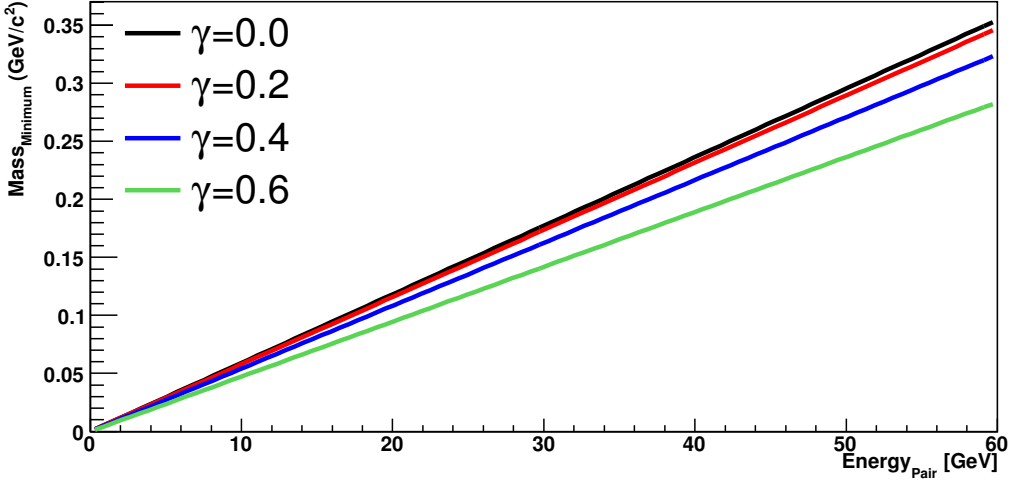


Figure 21: Yaxis: minimum pair mass, Xaxis: Pair energy. Different curves are for different energy asymmetry cuts. Note: figure assumes zvertex of collision is at zero. Some spread is possible as the collision moves either nearer or further from the detector.

of cluster 1 and 2 are uncorrelated¹ and derive the the equation for the fractional mass resolution we get²:

$$\frac{\delta m}{m} = \frac{1}{2} \left(\frac{\delta E_1}{E_1} \oplus \frac{\delta E_2}{E_2} \oplus \frac{\delta\theta}{\tan(\frac{\theta}{2})} \right) \quad (11)$$

The $\delta\theta$ term can be approximated in terms of the cluster position resolution, δx and the vertex position resolution δz as:

$$\theta^2 \approx \frac{(x_1 - x_2)^2 + (y_1 - y_2)^2}{z^2} \quad (12)$$

with its resolution

$$\delta\theta \approx \frac{\sqrt{2}\delta x \oplus \theta z}{z} \quad (13)$$

Plugging in some typical values (2 cm zvertex resolution, 2 mm cluster position resolution, 8 cm cluster separation) into equation 13 gives the angular resolution as: $7.37 \oplus 1.89$ hundredths of a degree. Continuing the chain back to fractional mass resolution shows that the angular resolution contributes around 3.5% of degradation. This number scales roughly in proportion to 1/distance between the clusters. Therefore, we expect for the fractional mass resolution to degrade at high energies. This is contrary to our normal expectations, based on the energy resolution, that calorimeter performance increases with energy.

Plugging equation 10 into equation 11 gives:

$$\frac{\sigma(m)}{m} = \frac{1}{2} \sqrt{a^2 \left(\frac{1}{E_1} + \frac{1}{E_2} \right) + b^2 \left(\frac{1}{E_1^2} + \frac{1}{E_2^2} \right) + 2c^2} \quad (14)$$

¹not the case in the event of common mode noise

²We omit the line widths since they are ~ 1 keV.

which can be expressed in terms of the pair energy and asymmetry:

$$\frac{\sigma(m)}{m} = a \frac{1}{\sqrt{1-\gamma^2}} \frac{1}{\sqrt{E_{pair}}} \oplus b \sqrt{\frac{1+\gamma^2}{2}} \frac{1}{1-\gamma^2} \frac{1}{E_{pair}} \oplus c \frac{1}{\sqrt{2}} \oplus \frac{\delta\theta}{2 \tan(\frac{\theta}{2})} \quad (15)$$

We equation 15 and plots of the fractional mass resolution to estimate the energy resolution in section 6.5. We use the η meson and not the π^0 to reduce effects from two-photon merging.

6.3 Identification of mis-calibrated towers

In the central arm bad towers are flagged by looping over all clusters meeting a minimum energy threshold, finding each cluster’s central tower and counting the number of times each tower is hit. The hits are expected to be distributed evenly between all towers in the central arm³. Towers with too few or too many counts relative to the other towers in the EMC are placed in a “warnmap”.

A procedure similar in spirit is carried out in the MPC, but we have the complication that hits are not expected to be distributed amongst all towers evenly. There are a number of competing effects which determine the hit distributions. The input flux of particles is determined using $dN/d\eta$, but each tower integrates over this distribution according to their span in $\Delta\phi$. Towers closer to the beampipe have a larger span than towers farther out from the beampipe. The hit distribution is plotted in figure 22 and the masked off towers are shown in their approximate positions around the beampipe in figure 23.

We loop over all clusters meeting several energy thresholds and count the number of times each central is hit. Then for each energy threshold, the number of hits is plotted against the tower radius. The correlation plot is fit with a first degree polynomial using an LTS regression to remove outliers from the fit. Hot and cold towers are defined as lying beyond 3.2 sigma of the central fit value.

³There is a trivial modification between the PbSc and PbGl since the PbSc towers are larger in $d\eta \times d\phi$ space than the PbGl towers.

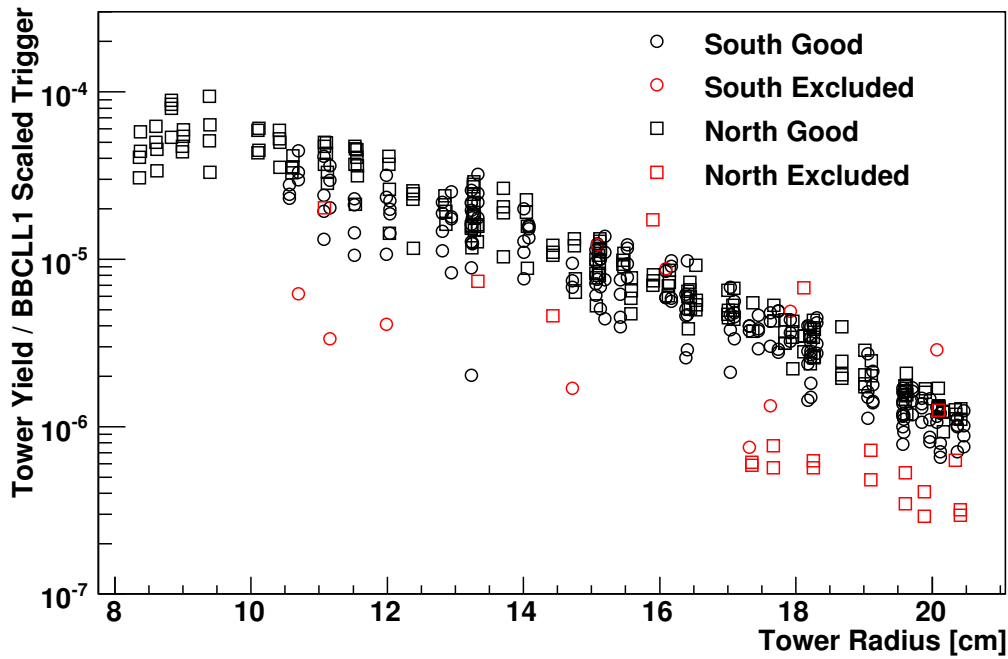


Figure 22: Yaxis: \log_{10} (Normalized counts), Xaxis: Tower radial position from beampipe center [cm]. Excluded towers are shown in red and good towers are shown in black.

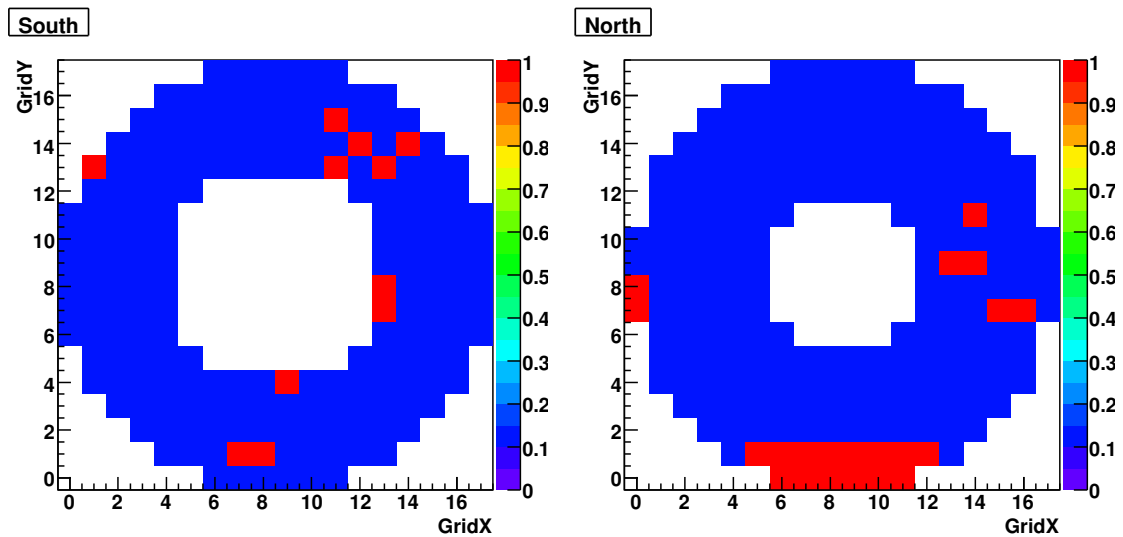


Figure 23: MPC warnmap drawn in the approximate tower locations. Blue good tower, Red included in warnmap.

6.4 π^0 and η identification

Two photon invariant mass peaks are formed from the minimum bias and MPC triggered data datasets. Events are required to have a vertex between ± 30 cm. The following cuts are placed on clusters:

- **Photonic cluster** `mpcClusterContent::chi2core()<2.5`
- **Minimum energy** `mpcClusterContent::ecore()>2 [GeV]`
- **Warnmap veto** towers flagged as either hot or cold are removed from analysis. In addition, towers screened by the beam pipe support in the north arm are removed from analysis
- **Radius cut** The reconstructed clusters are required to have a radial position between 13 and 18 cm from the center of the beampipe.

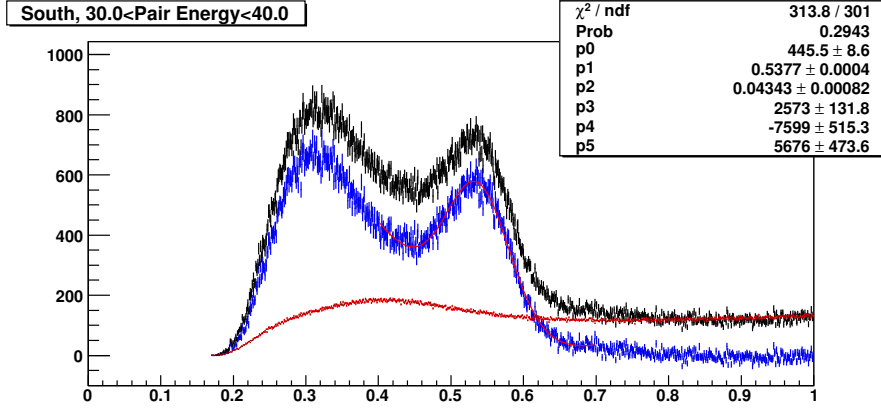
and on pairs of clusters

- **Pair separation** clusters must be separated by more than 2.6 cm
- **Same arm** clusters must be from the same arm
- **Energy asymmetry** must be less than 0.6 for good pairs
- **TDC Timeout** The TDC of the cluster's central tower must be less than the TDC timeout value

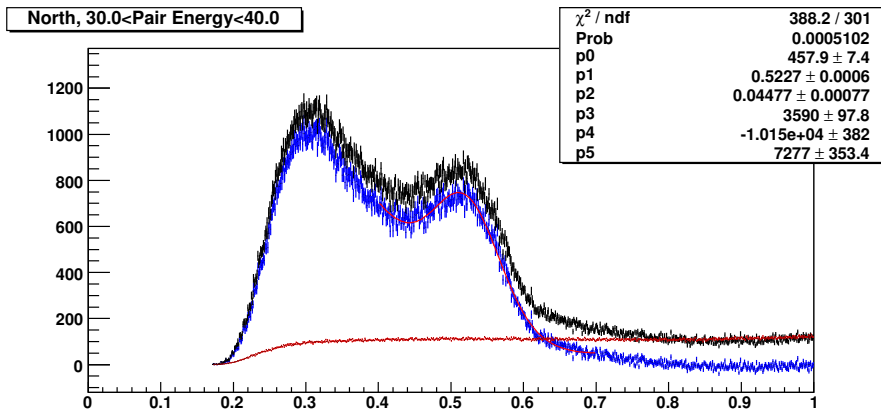
Event mixing is done to determine the combinatorial background shape. The event mixing forms a pool of clusters and their associated vertices. Once the pool is filled, the foreground clusters are mixed across random clusters from the pool with the restriction that the zvertex difference between the foreground and background be less than 2 cm. The background mass distribution is normalized to the foreground mass distribution in the window between 0.3 (0.7) to 1.0 GeV/c^2 for the π^0 (η). The $M_{\gamma\gamma}$ distributions and fits to the η meson peak are shown in figure 24 for the 30-40 GeV pair energy interval. The distributions over a wide range of energy and for both the triggered and minimum bias data sets are available in appendices B-E. The properties of the π^0 peaks are provided in figure 33 and for the η in . By virtue of the larger opening angle, the η peak properties are relatively stable versus energy.

6.5 Fractional mass resolutions from data

The fractional mass resolutions are shown in figure 26 for both the Minimum bias and MPC triggered datasets. Both sets of mass resolutions are flat and around $\sim 5\%$. The energy asymmetry does not affect the mass resolutions. Therefore, at these energies the angular resolution and constant terms dominate equation 15. If we assign $\sim 3.5\%$ (explained in section 6.2) to the angular resolution term, we can assign the rest to the



(a) South Arm



(b) North Arm

Figure 24: Yaxis: Counts, Xaxis: $M_{\gamma\gamma}$ for cluster pairs with energy between 30 and 40 GeV. Foreground (black), scaled mixed (red) and subtracted (blue) distributions are shown. The subtracted distribution is fit to a Gaussian distribution (parameters 0, 1 and 2) plus a second degree polynomial (parameters 3, 4 and 5). The mixed event distribution is normalized to the foreground distribution in the mass window 0.7 to 1.0 GeV/c^2 . Data is aggregated over all disk-resident run8pp data and all MPC triggers. The plots show a clear η peak.

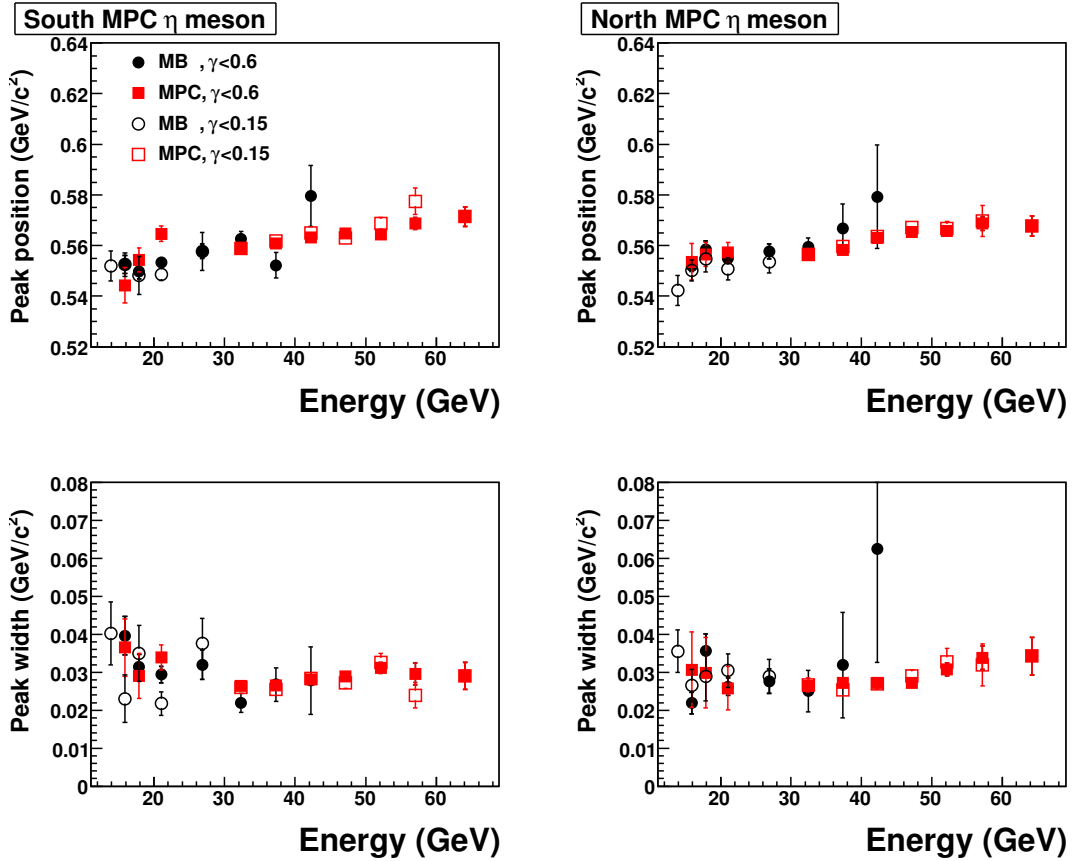


Figure 25: The positions and widths of the η meson peaks extracted in bins of energy. Points are plotted at the mean energy in each bin. Points for energy less than or greater than 30 GeV are from minimum bias and MPC triggered data respectively. Open (closed) points are generated with pairs with energy asymmetry less than 0.15 (0.6).

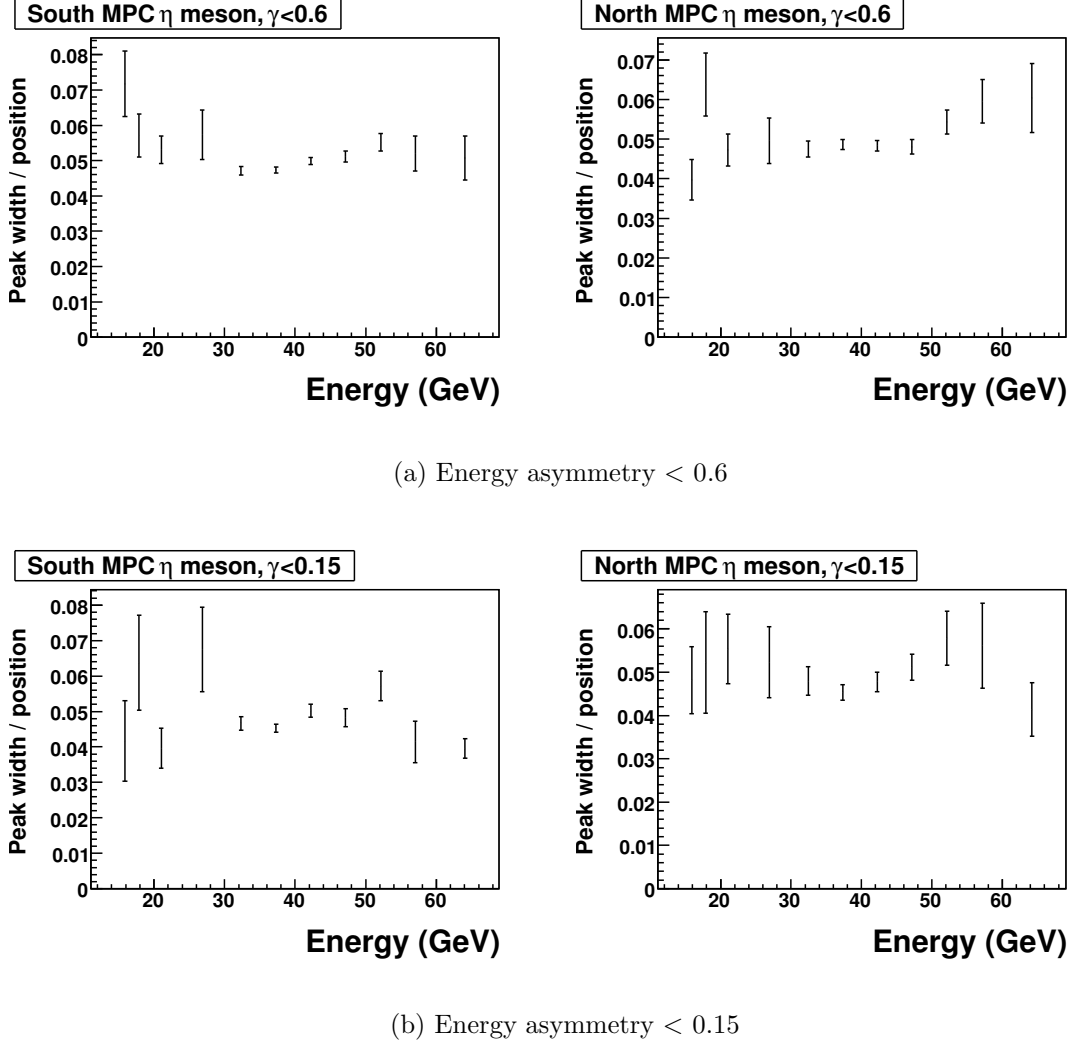


Figure 26: The widths divided by positions of the η meson peaks extracted in bins of energy from both the Minimum Bias and MPC triggered datasets. Points are plotted at the mean energy in each bin. The fractional mass resolution does not depend strongly with the energy asymmetry indicating that the constant terms dominate in equation 15

constant term. Therefore, we expect that the energy constant term to be approximately 5%⁴.

6.6 Gain stability

To check the stability of the gain, peaks are extracted in the same fashion as shown in figure 24 on a fill-by-fill basis. The extracted peak positions are shown in figure 27.

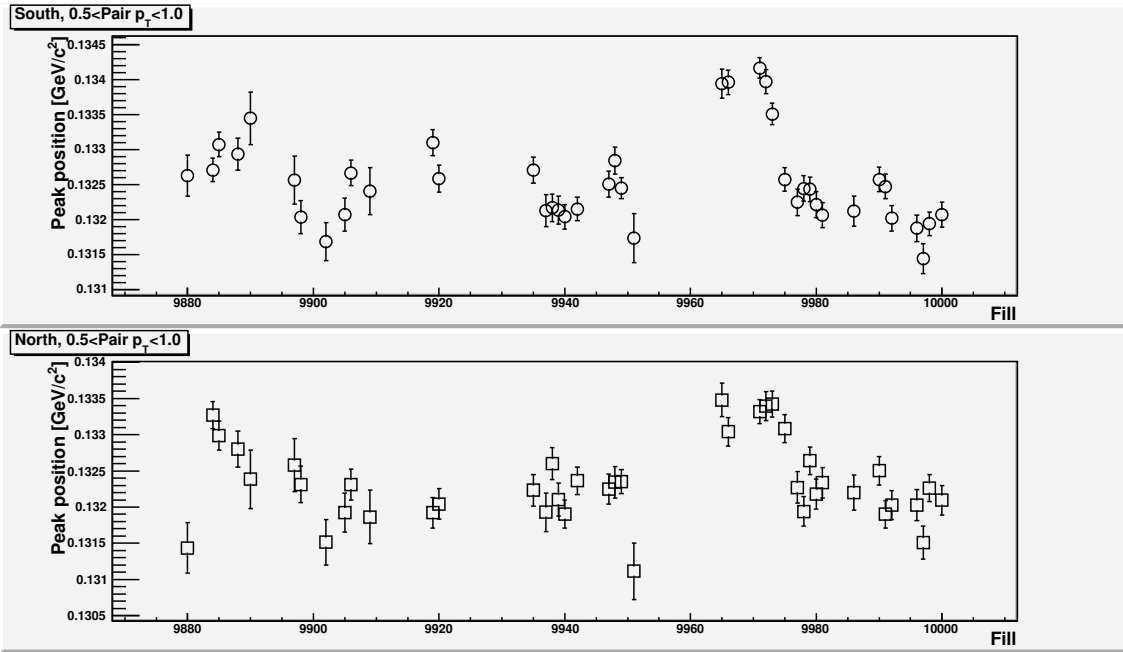


Figure 27: Yaxis: π^0 peak position for pairs with p_T between 0.5 and 1.0 GeV/c, Xaxis: fill number. Top: South arm, Bottom: North arm.

6.7 Comparison to Monte-Carlo

If we only used a single energy bin, an infinite set of (a,b,c) would be able to match the measured mass resolution. Therefore, we extract peak widths as a function of the pair energy with the goal to pick the cluster energy resolution which best matches data. The π^0 and η meson peak positions as reconstructed by our detector are not required to sit at the PDG value. Acceptance and reconstruction effects can shift the peak value away from the expected location. For example, in the PHENIX central arms the π^0 peak is expected to change with p_T [4].

The simulation is done in two steps. The first step's goal is to find the correct set of noise terms which describe the MPC data. This effect of mis-calibration and noise is studied by comparing the mass peak widths from data and from various simulation sets

⁴The total and angular fractional **mass** resolutions are approximately 5% and 3.5%, respectively. Therefore, the remaining noise is: $\sqrt{5\%^2 - 3.5\%^2}$. Then we multiply by the $\sqrt{2}$ in formula 15 to get the **energy** resolution term.

Meson	Trigger	Energy (GeV)
π^0	Minimum bias	9 - 11
π^0	Minimum bias	11 - 13
π^0	Minimum bias	13 - 15
π^0	Minimum bias	15 - 17
π^0	Minimum bias	17 - 19
η	MPC	15 - 17
η	MPC	17 - 19
η	MPC	19 - 25
η	MPC	25 - 30
η	MPC	30 - 35
η	MPC	35 - 40

Table 1: Mesons and associated energy ranges to be compared between data and Monte-Carlo.

where noise terms are introduced at the tower level. The second step is to compare the absolute peak position between data and simulation where the simulation peak position is taken from the simulation set whose peak width best matches that from data.

The simulation data was generated using a PHPythia and TuneA with processes: 11, 12, 13, 28, 53, 68 and 96 turned on and with a CKIN(3) cut of 2.0 GeV/c. This tune is bench marked against all measured RHIC cross-sections at $\sqrt{s} = 200$ GeV in reference [3]. The simulation chain is the standard PHPythia, PISA, p2DST with zvertex smearing. The produced DST's contain **raw tower** information only. Calibrated towers and clusters are produced on the fly as analyzers iterate over the simulated DST's. This flexibility allows us to introduce noise and mis-calibrations in an arbitrary fashion at the tower level. By default the simulation code uses perfect tower gains and 75 MeV electronics noise. Comparison to data is only done using Minimum Bias triggered data.

The peak values and widths for π^0 and η mesons were extracted in a 10x10 grid of grid of constant and noise energy resolution terms. The constant term was varied between 0 and 18% in steps of 2%. The electronics noise was set 75 MeV, and with the following levels added in quadrature 0, 25, 50, 75, 100, 125, 150, 200, 300 and 400 MeV.

The same reconstruction, analysis, and peak extraction code described in 6.4 was used on the simulated data. Comparison between simulation and data are done using bins of energy. Energy is the most natural variable for exploring potential effects from cluster merging. Similarly, using π^0 's or η 's for comparison only make sense in certain energy ranges. The list of energies and mesons to be compared are listed in table 1.

The mass distributions for π^0 and η are show in the appendices B-E As an example, some mass distributions from data and from simulation are provided in figure 28.

The data may have a global scale offset from the true calibrations. Therefore, we divide out any potential scale factors by comparing the meson peak width divided by the position. Comparison between data and the 100 noise settings is show in figures 29 and 30 for the south and north arms respectively.

To choose the optimal combination of constant and noise energy resolution param-

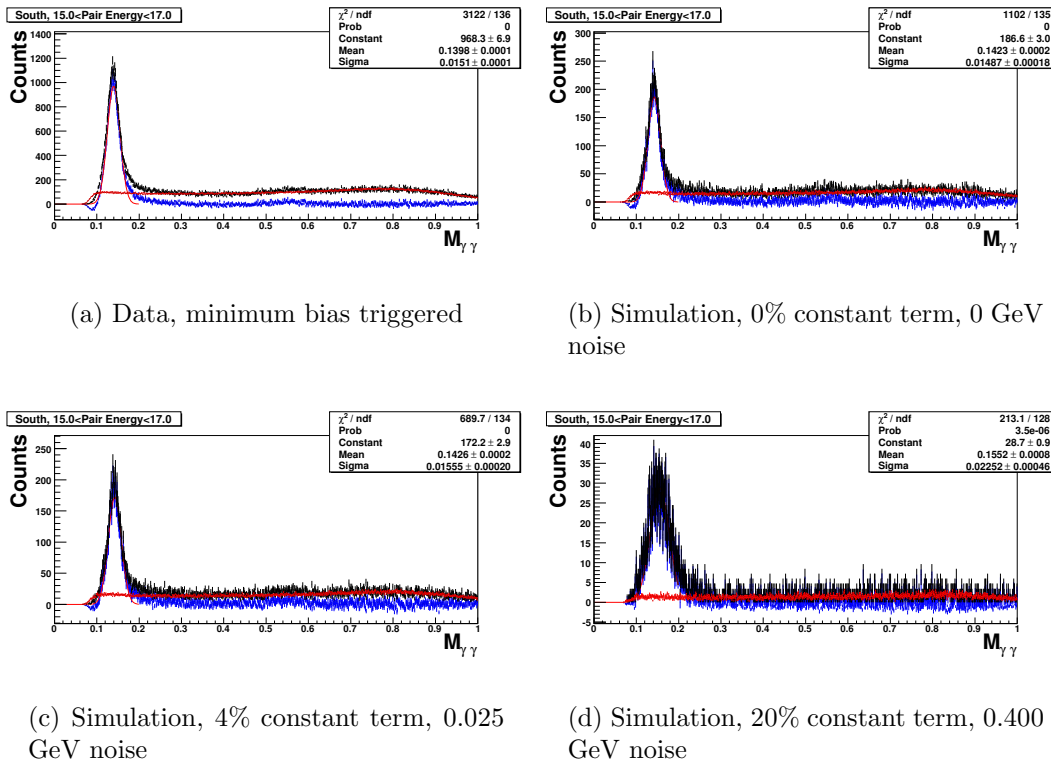


Figure 28: $M_{\gamma\gamma}$ distributions for the MPC from data and simulation. Arm: South, $15 < \text{Energy} < 17$ GeV. Each plot shows the foreground (black), mixed event (red) and subtracted (blue) mass distribution.

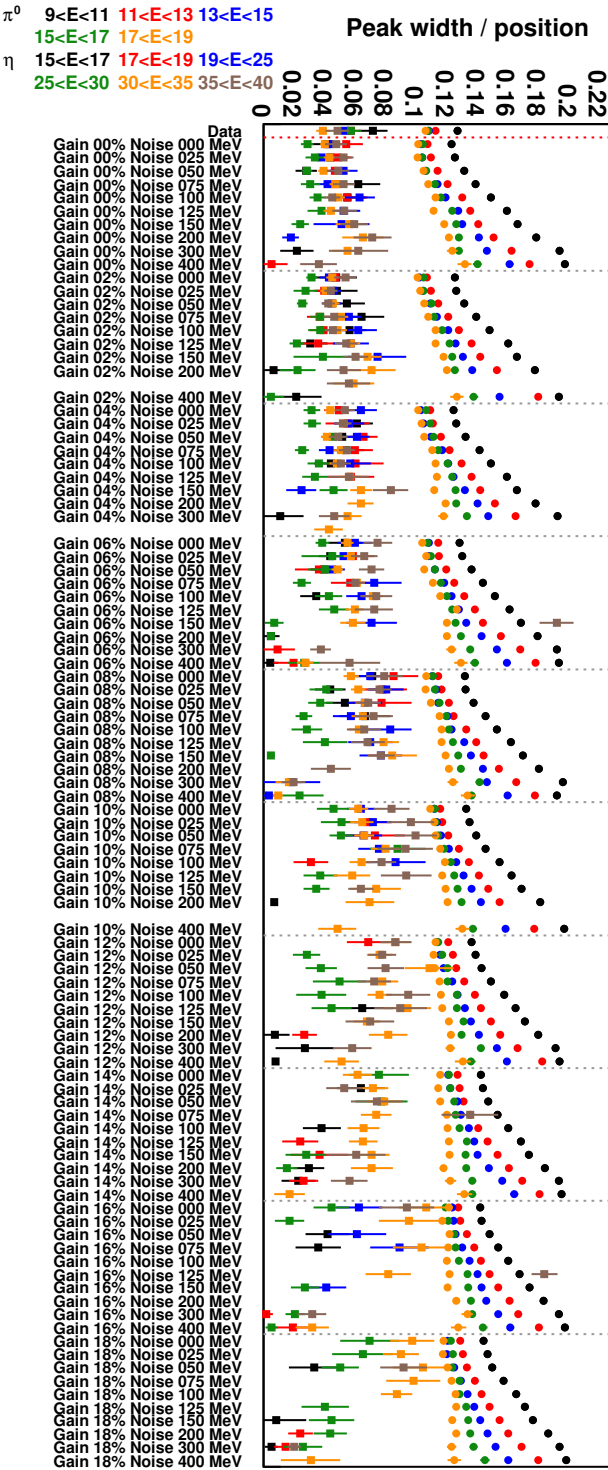


Figure 29: Peak widths / peak positions in various kinematic bins for the South MPC

eters, we calculate the χ^2 between data and simulation for each combination of noise. Results are shown in figures 31 and 32 respectively. Three χ^2 values are presented for

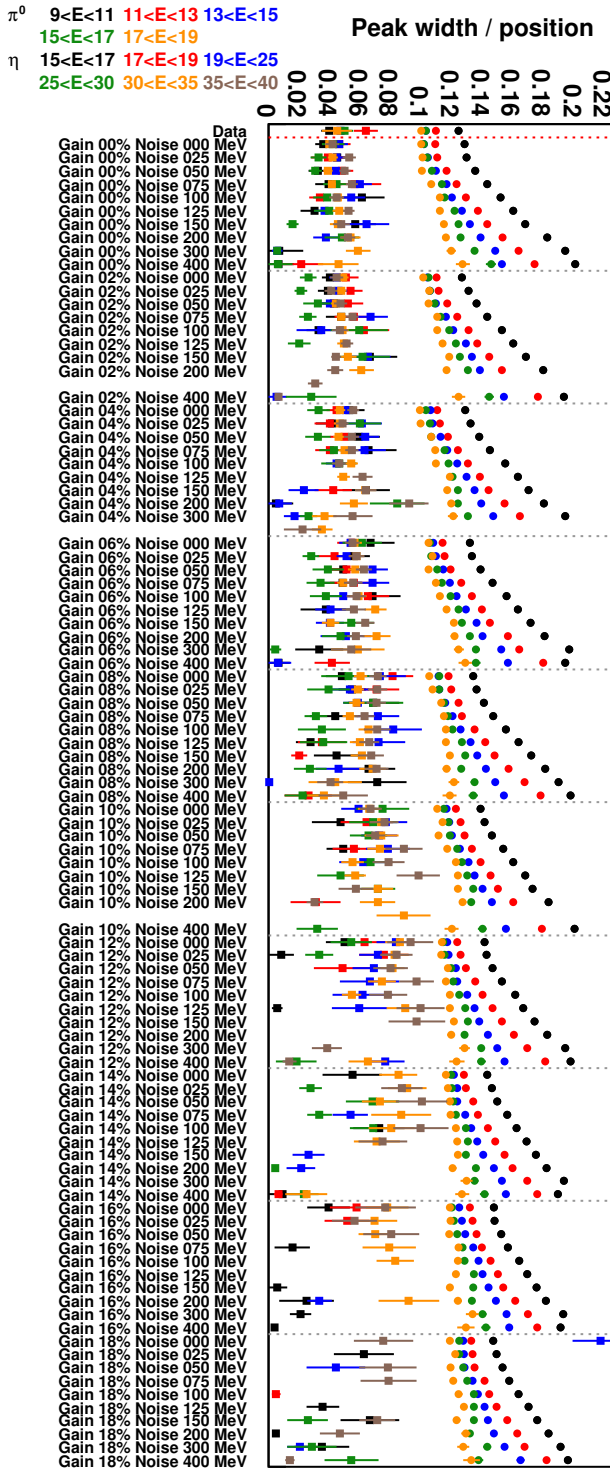


Figure 30: Peak widths / peak positions in various kinematic bins for the North MPC

each noise setting: π^0 alone, η alone and for both.

The best noise setting is 4% constant, and 25 \oplus 75 MeV noise. The constant term

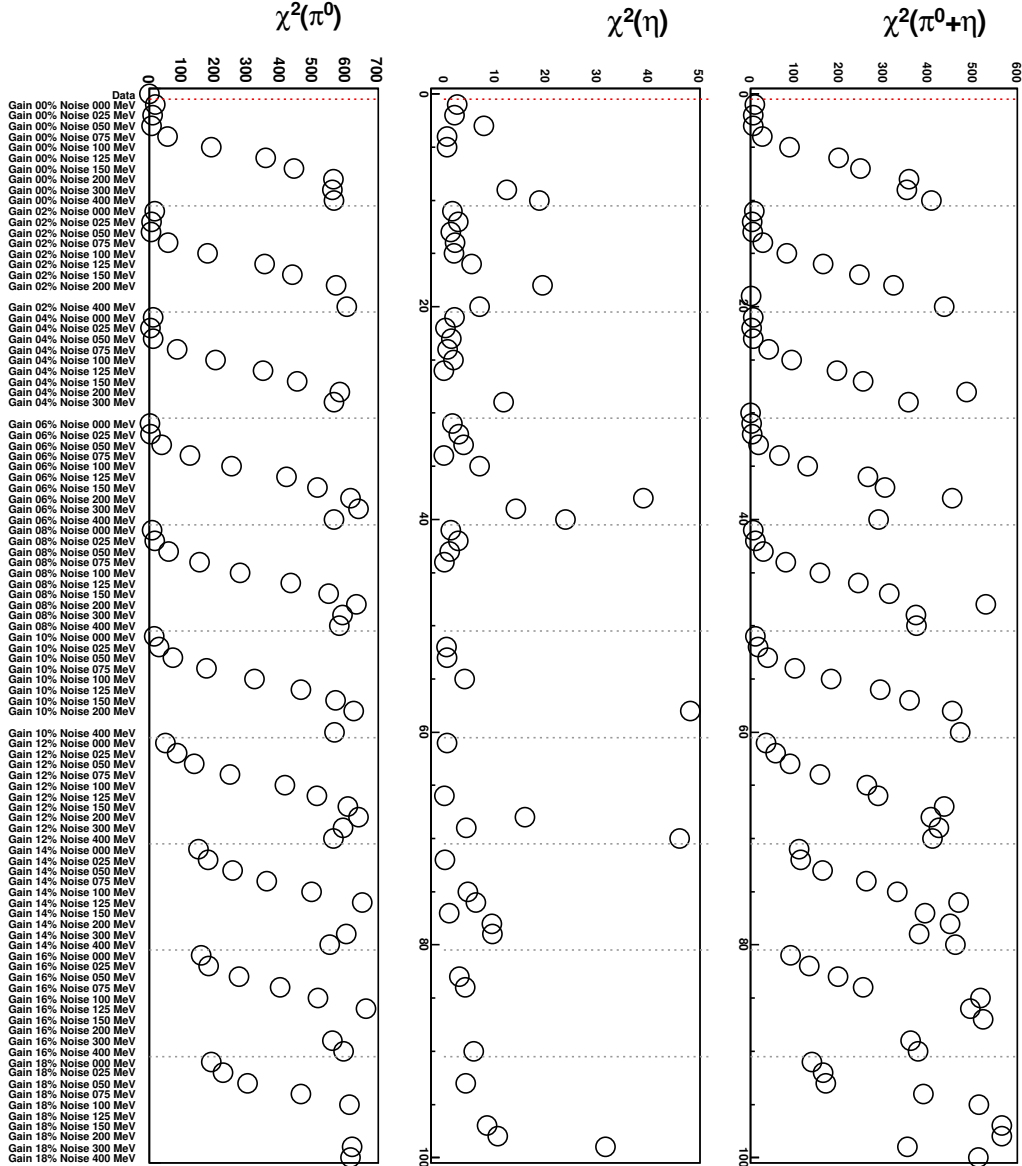


Figure 31: The reduced χ^2 values of the difference between the data and simulation peak widths / positions. Five kinematic bins are used for the π^0 and six for the η . The reduced χ^2 values are presented separately for the π^0 (left), η (middle) and the sum (right). Values are from the South MPC.

agrees with the rough determination of section 6.5.

The peak properties for the π^0 and η are shown in figure 33. There is tension between the π^0 and η peak positions at the $\pm 2\%$ level between both the North and South arms. We therefore assign it as the systematic error for the global energy scale.

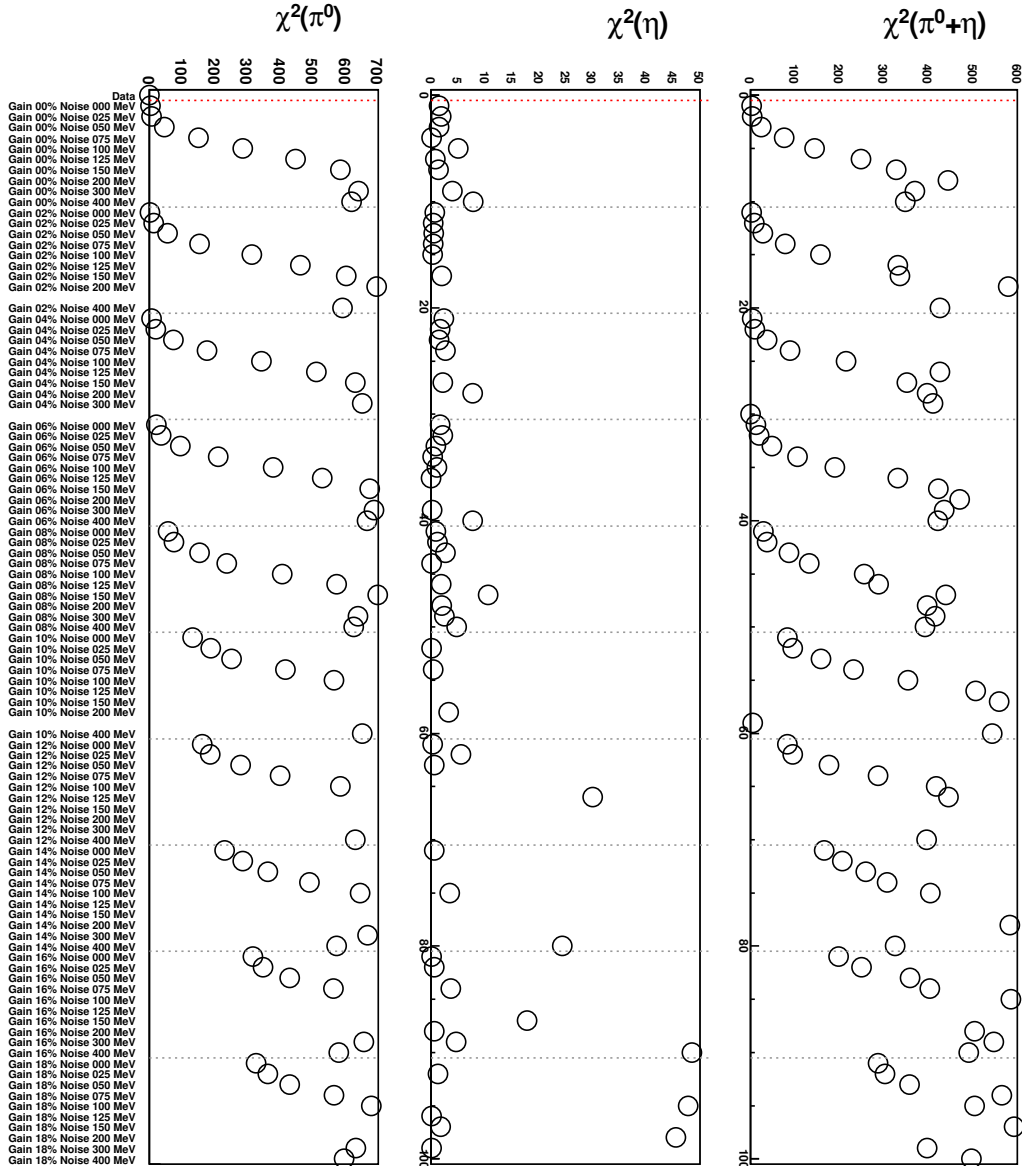
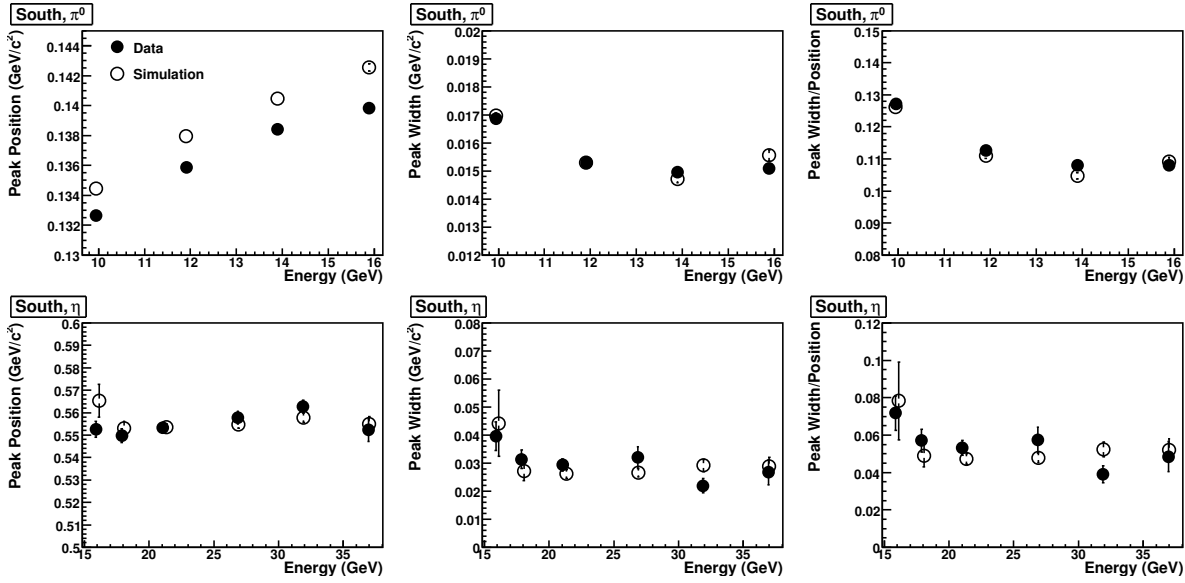
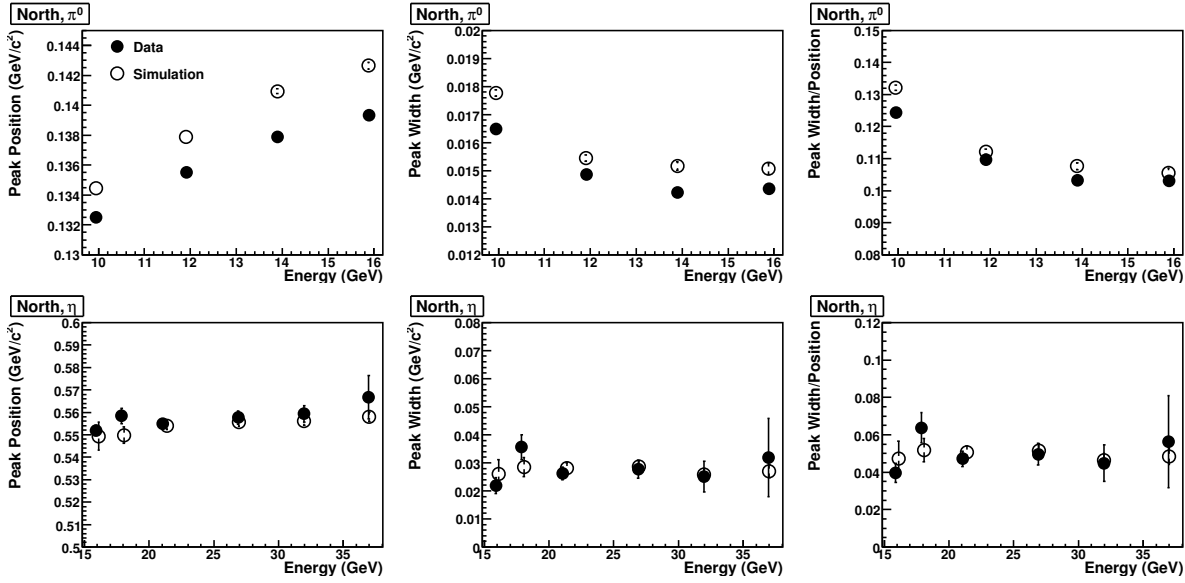


Figure 32: The reduced χ^2 values of the difference between the data and simulation peak widths / positions. Five kinematic bins are used for the π^0 and six for the η . The reduced χ^2 values are presented separately for the π^0 (left), η (middle) and the sum (right). Values are from the North MPC.



(a) South



(b) North

Figure 33: The peak properties for the π^0 and η from Minimum Bias triggered data and simulation (with a 4% constant term + 90 MeV of noise).

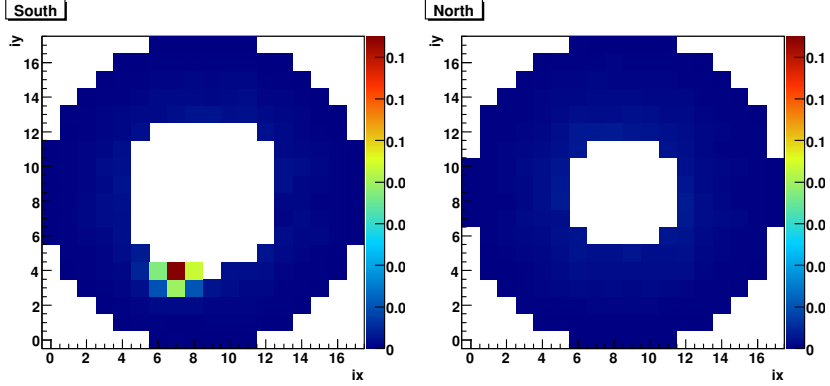
References

- [1] O. Eysen *et al.* PHENIX Analysis Note 596
- [2] J. Koster *et al.* PHENIX Technical Note 440
- [3] J. Koster *et al.* PHENIX Analysis Note 895
- [4] S. Bazilevsky *et al.* PHENIX Analysis Note 176
- [5] C. W. Fabjan and F. Gianotti, “Calorimetry for particle physics,” Rev. Mod. Phys. **75**, 1243 (2003).
- [6] J. Koster, https://www.phenix.bnl.gov/WWW/p/draft/jkoster4/mpc/tdc_overflow/

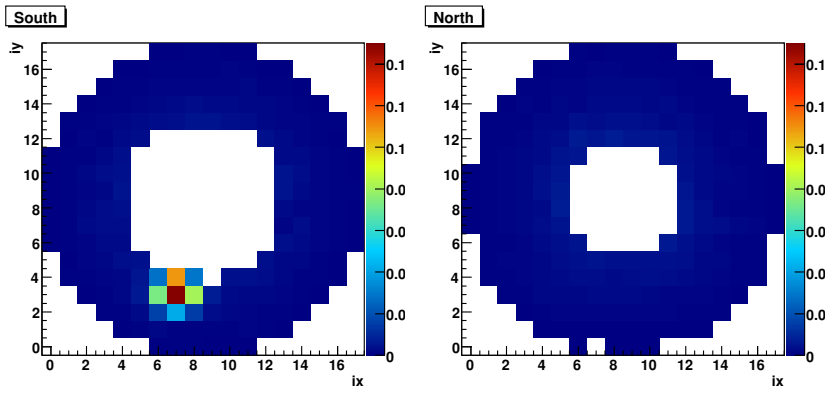
A Confirmation of Channel Mapping

Each tower is assigned a physical location in the reconstruction code. While the cables connecting each tower to its channel in the front end electronics are carefully checked for consistency, it is reassuring to check that the channel mapping is correct using data. The data method exploits energy deposition pattern from electromagnetic showers. If a photon deposits a large energy in a tower j , the electromagnetic shower will spread to its neighbors, depositing energy in them as well. Therefore, the analysis measures the conditional probability $P(i|j)$ for a tower i containing an energy deposit of 3 GeV or more, given that tower j has an energy deposit of 10 GeV or more. If towers i and j are neighbors the conditional probability will be high, and if they are not neighbors it will be low. For each tower, j , a plot is generated with the conditional probabilities for all other towers. The plot is drawn in the grid space of the previous section to clearly illustrate the effect. Two example plots are shown in figure 34.

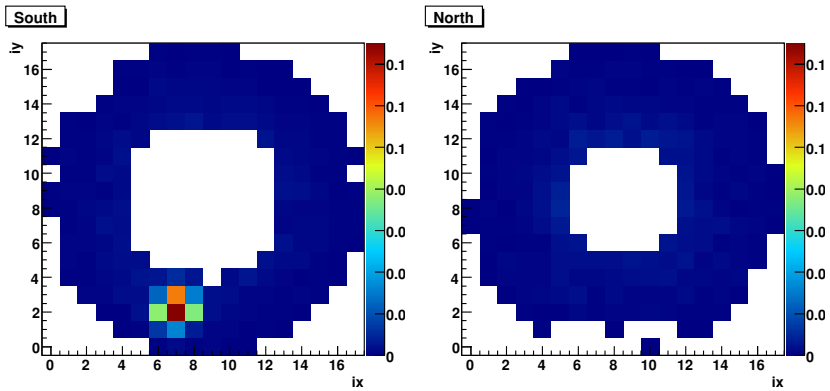
B $M_{\gamma\gamma}$ distributions binned in E_{pair} with η fit



(a) Tower j is located in the South Arm $(ix,iy)=(7,4)$



(b) Tower j is located in the South Arm $(ix,iy)=(7,3)$



(c) Tower j is located in the South Arm $(ix,iy)=(7,2)$

Figure 34: Z-axis: Conditional probabilities, $P(i|j)$, for tower i to contain more than 3 GeV given that tower j contains more than 10 GeV. Three sample towers are used for tower j . The fullscale of the z-axis goes to one since $P(j|j) \equiv 1$, but it is set to 15% to better see the neighboring tower's conditional probabilities.

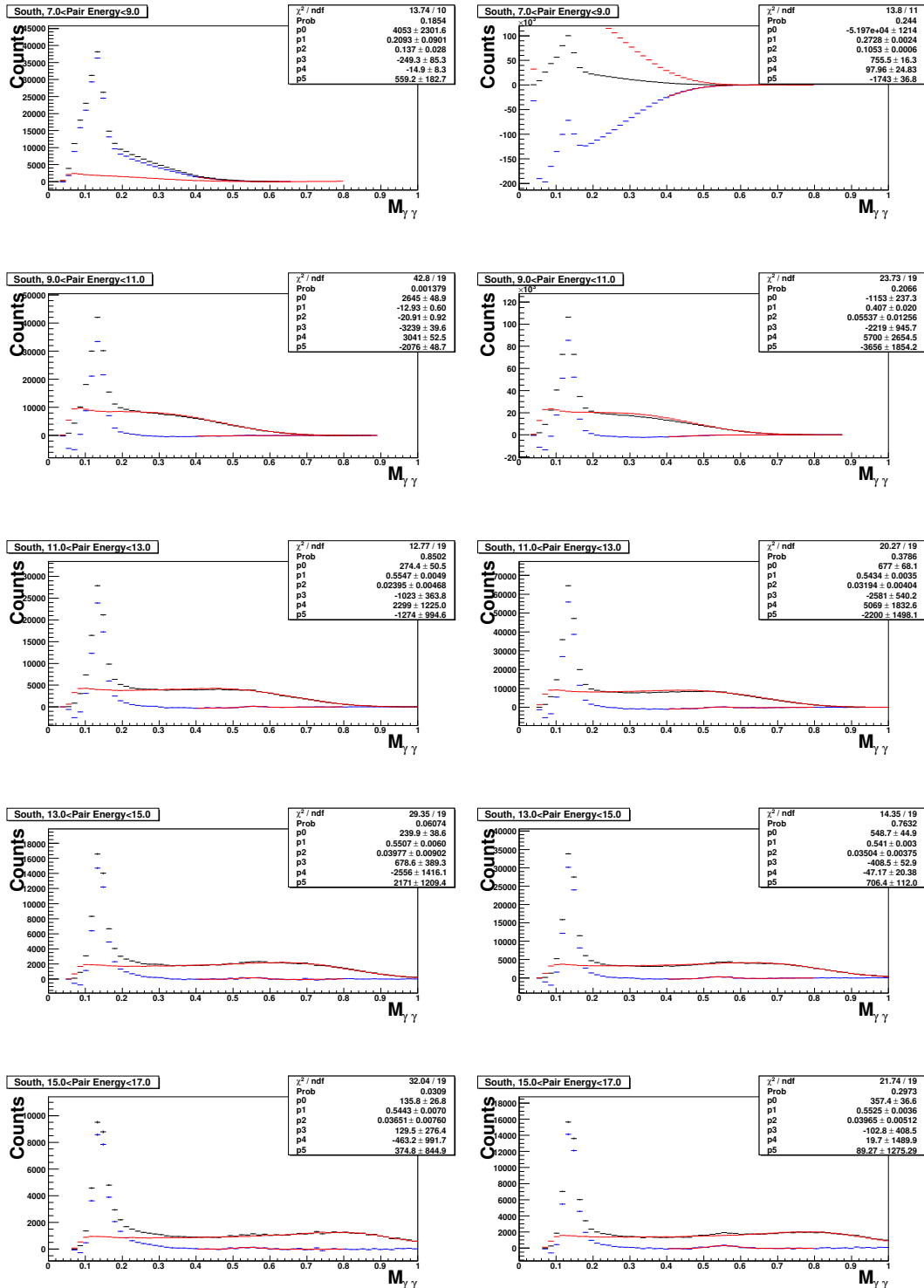


Figure 35: $M_{\gamma\gamma}$ distributions for MPC (left) and Minimum bias (right) triggered data for the South arm in bins of energy

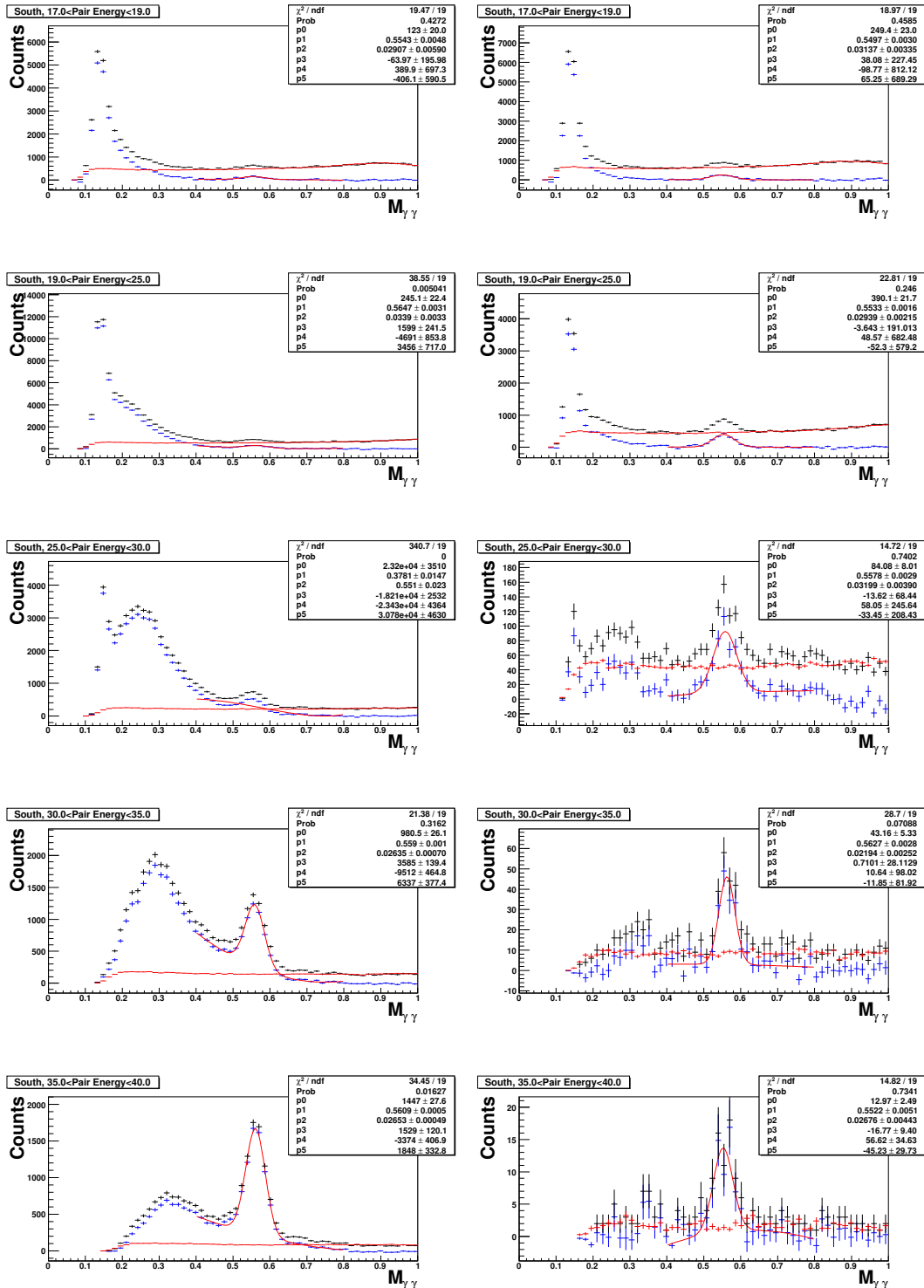


Figure 36: $M_{\gamma\gamma}$ distributions for MPC (left) and Minimum bias (right) triggered data for the South arm in bins of energy

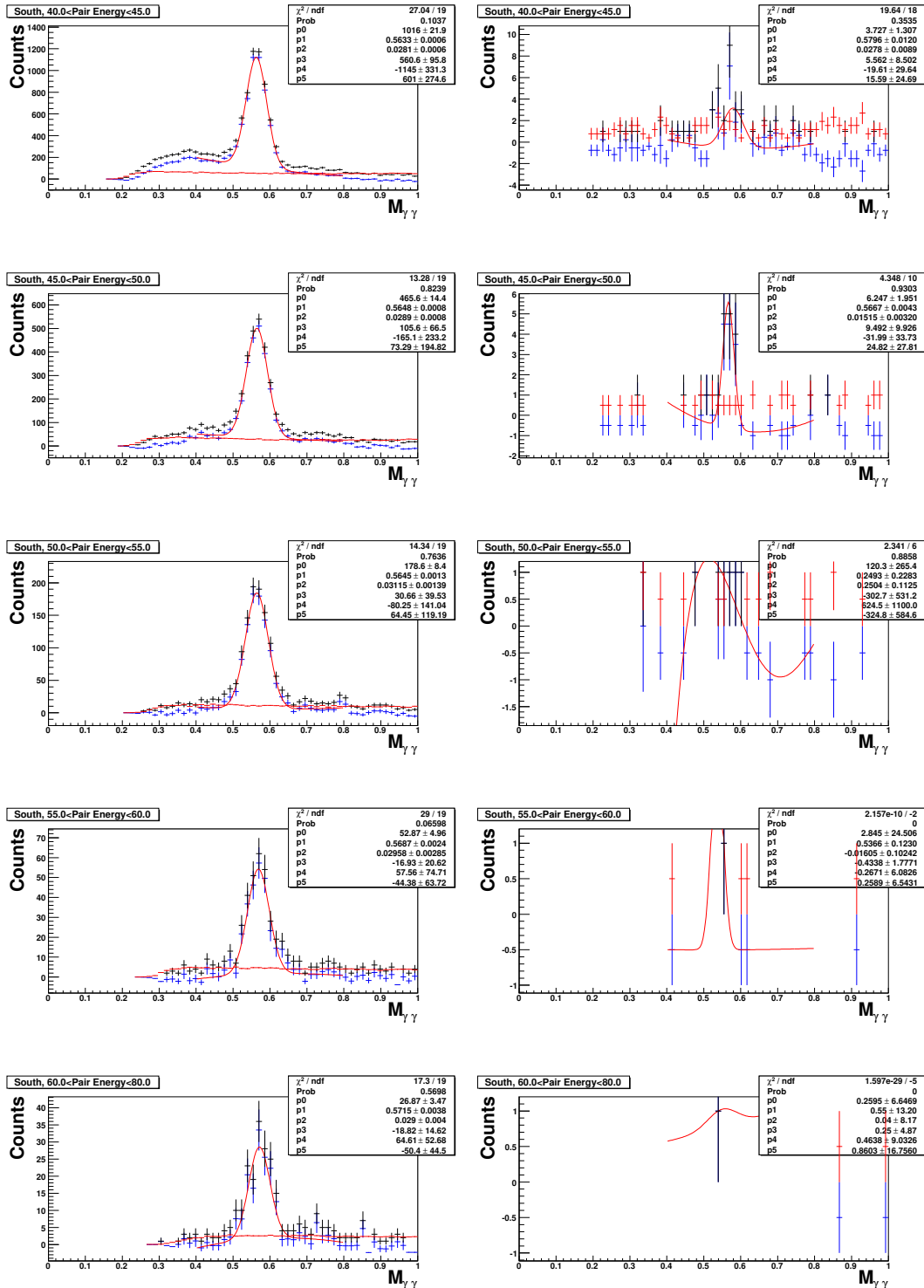


Figure 37: $M_{\gamma\gamma}$ distributions for MPC (left) and Minimum bias (right) triggered data for the South arm in bins of energy

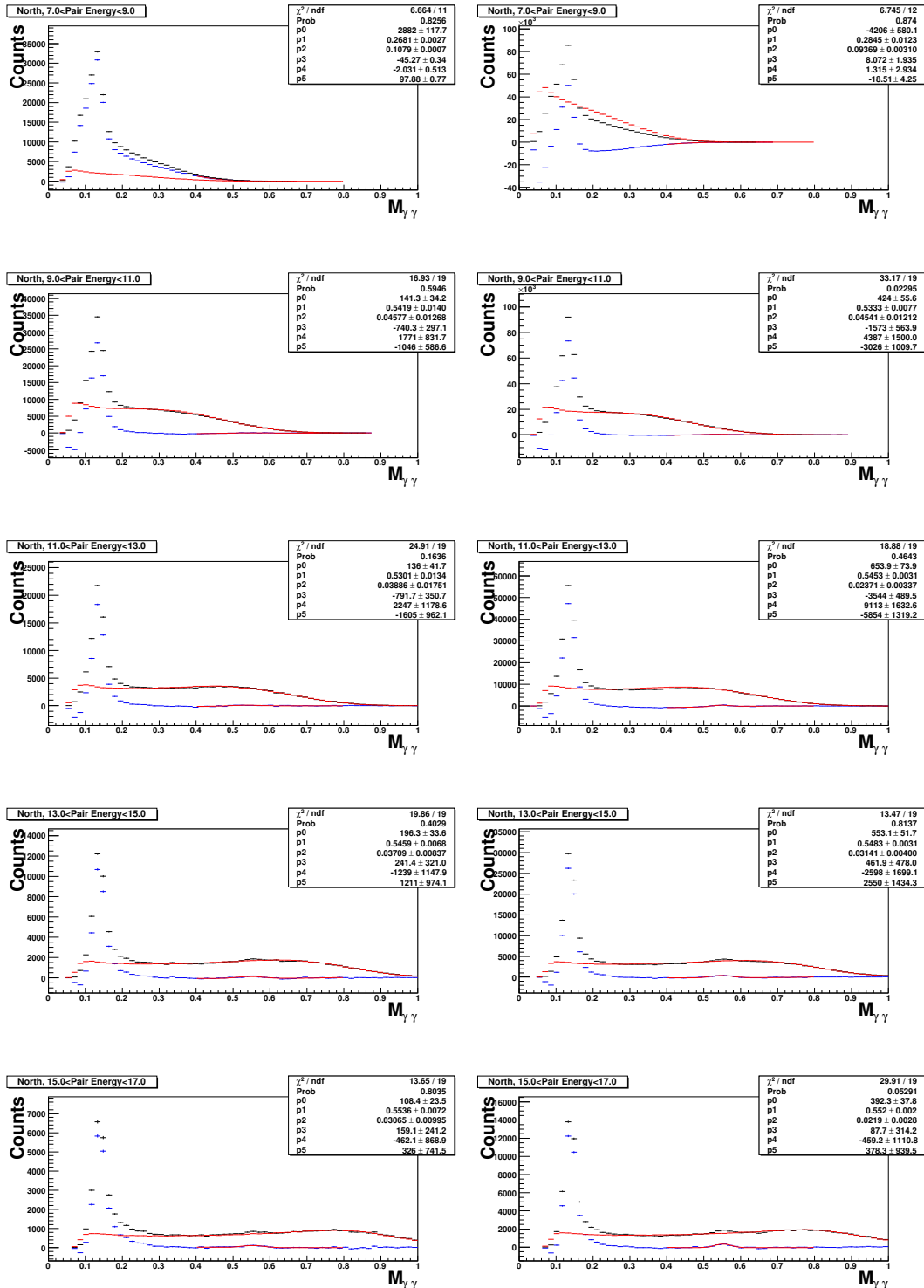


Figure 38: $M_{\gamma\gamma}$ distributions for MPC (left) and Minimum bias (right) triggered data for the North arm in bins of energy

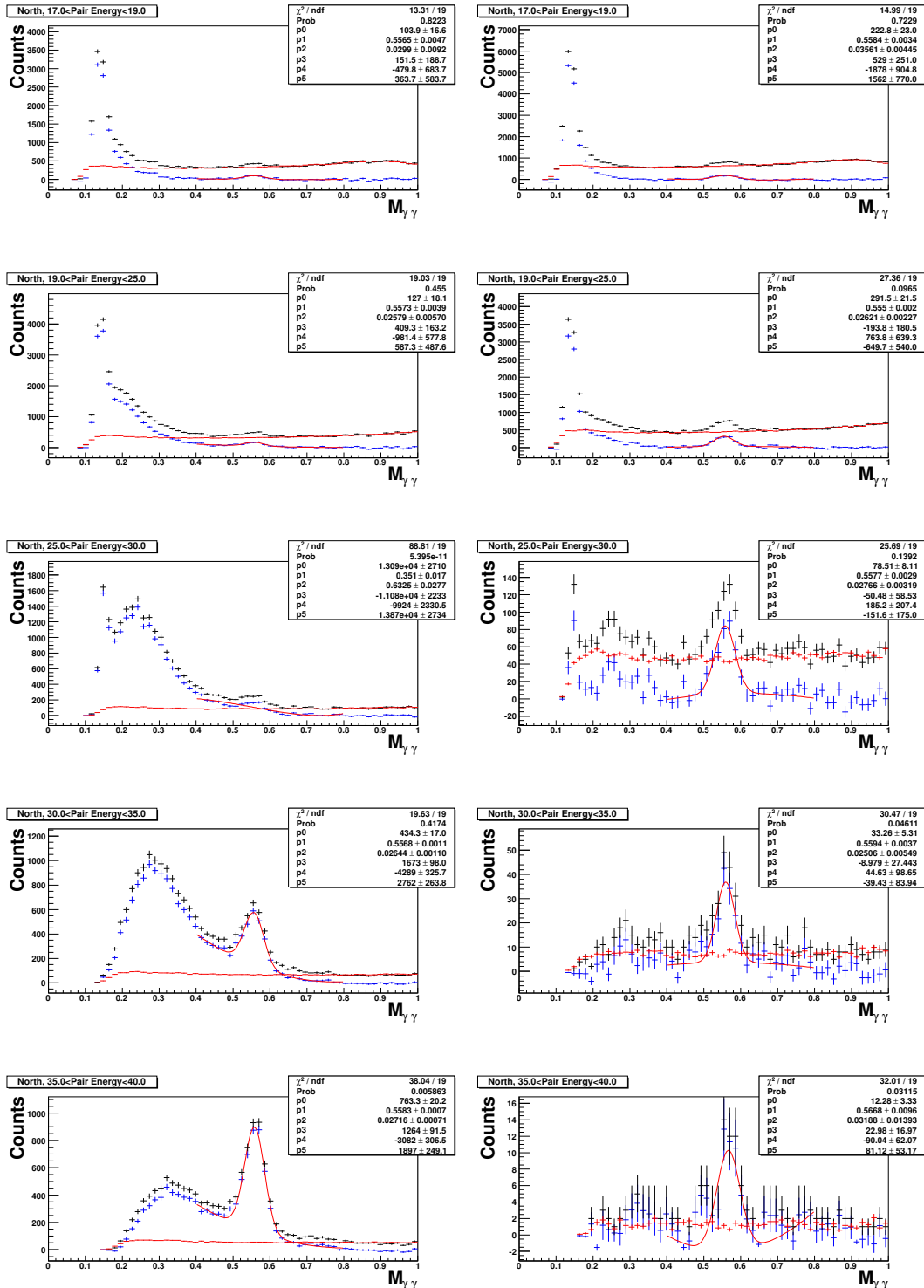


Figure 39: $M_{\gamma\gamma}$ distributions for MPC (left) and Minimum bias (right) triggered data for the North arm in bins of energy

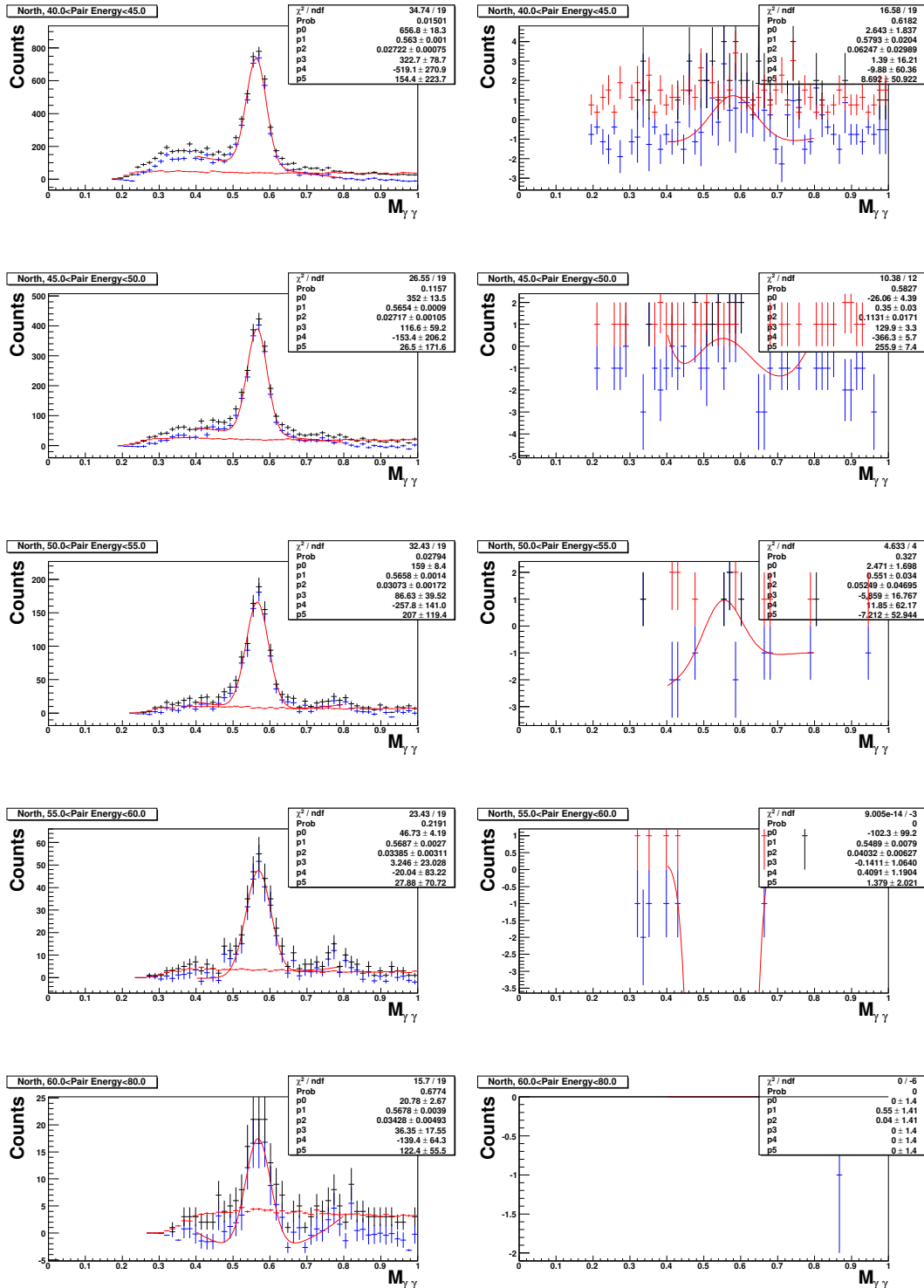


Figure 40: $M_{\gamma\gamma}$ distributions for MPC (left) and Minimum bias (right) triggered data for the North arm in bins of energy

C $M_{\gamma\gamma}$ distributions binned in $p_{T,pair}$ with η fit

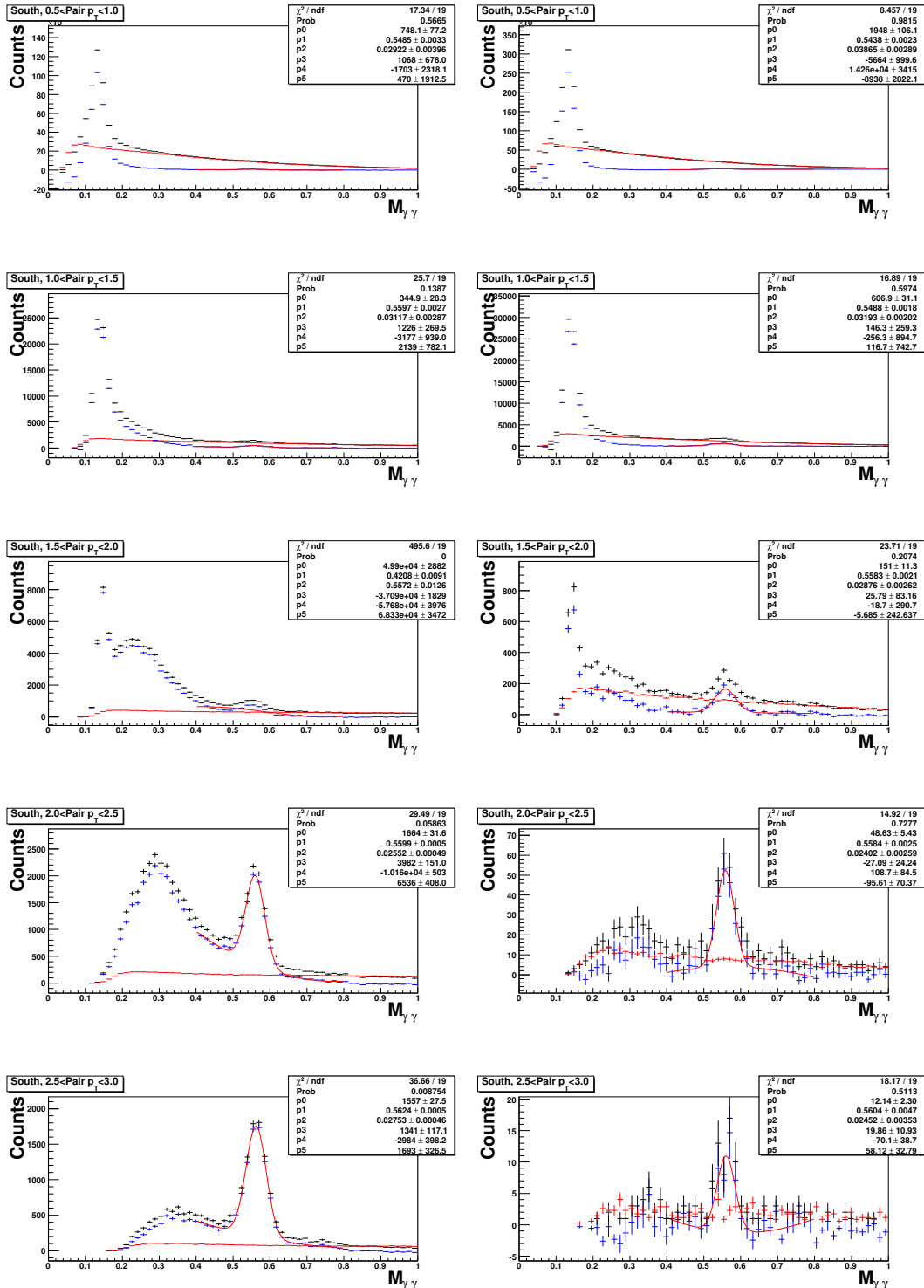


Figure 41: $M_{\gamma\gamma}$ distributions for MPC (left) and Minimum bias (right) triggered data for the South arm in bins of p_T

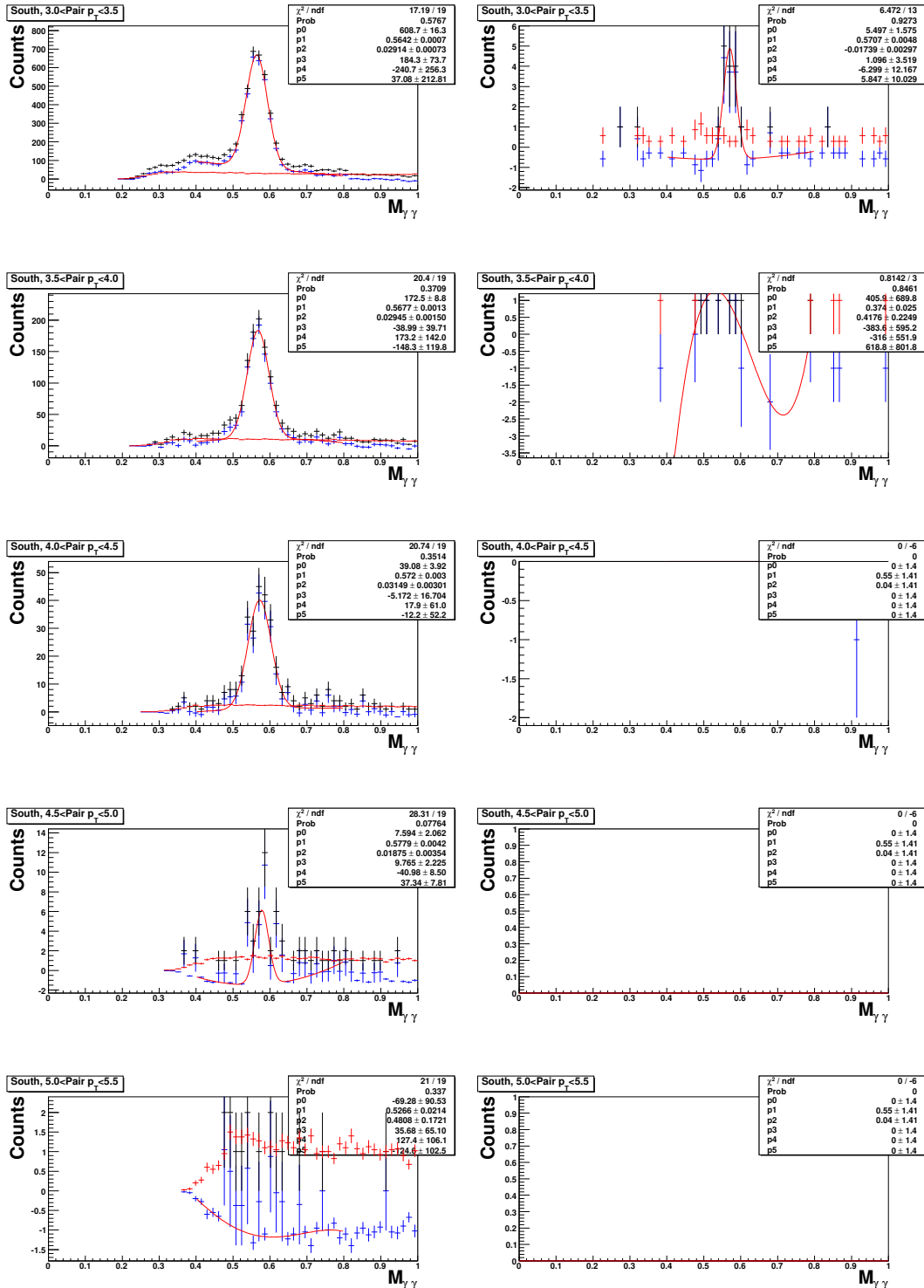


Figure 42: $M_{\gamma\gamma}$ distributions for MPC (left) and Minimum bias (right) triggered data for the South arm in bins of p_T

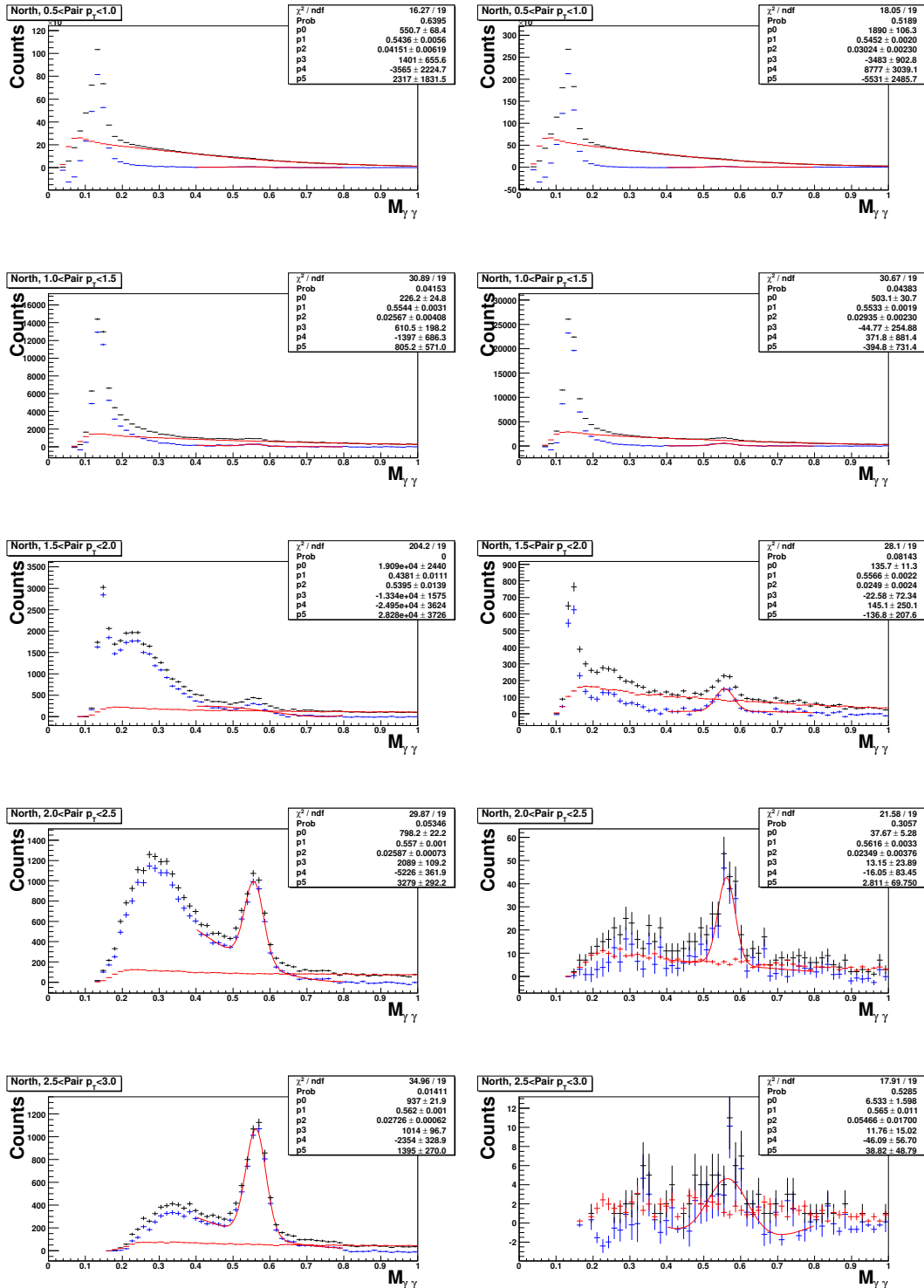


Figure 43: $M_{\gamma\gamma}$ distributions for MPC (left) and Minimum bias (right) triggered data for the North arm in bins of p_T

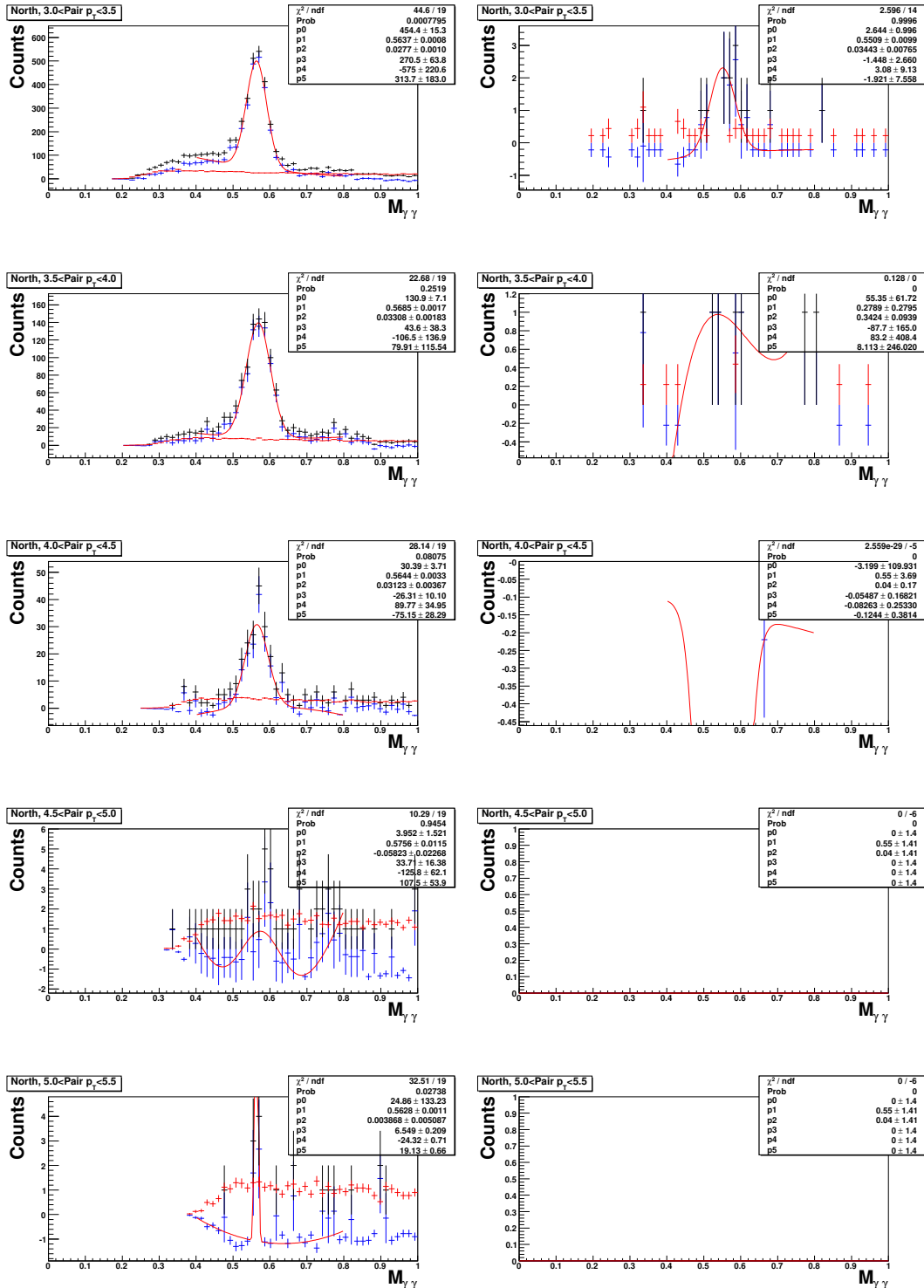


Figure 44: $M_{\gamma\gamma}$ distributions for MPC (left) and Minimum bias (right) triggered data for the North arm in bins of p_T

D $M_{\gamma\gamma}$ distributions binned in E_{pair} with π^0 fit

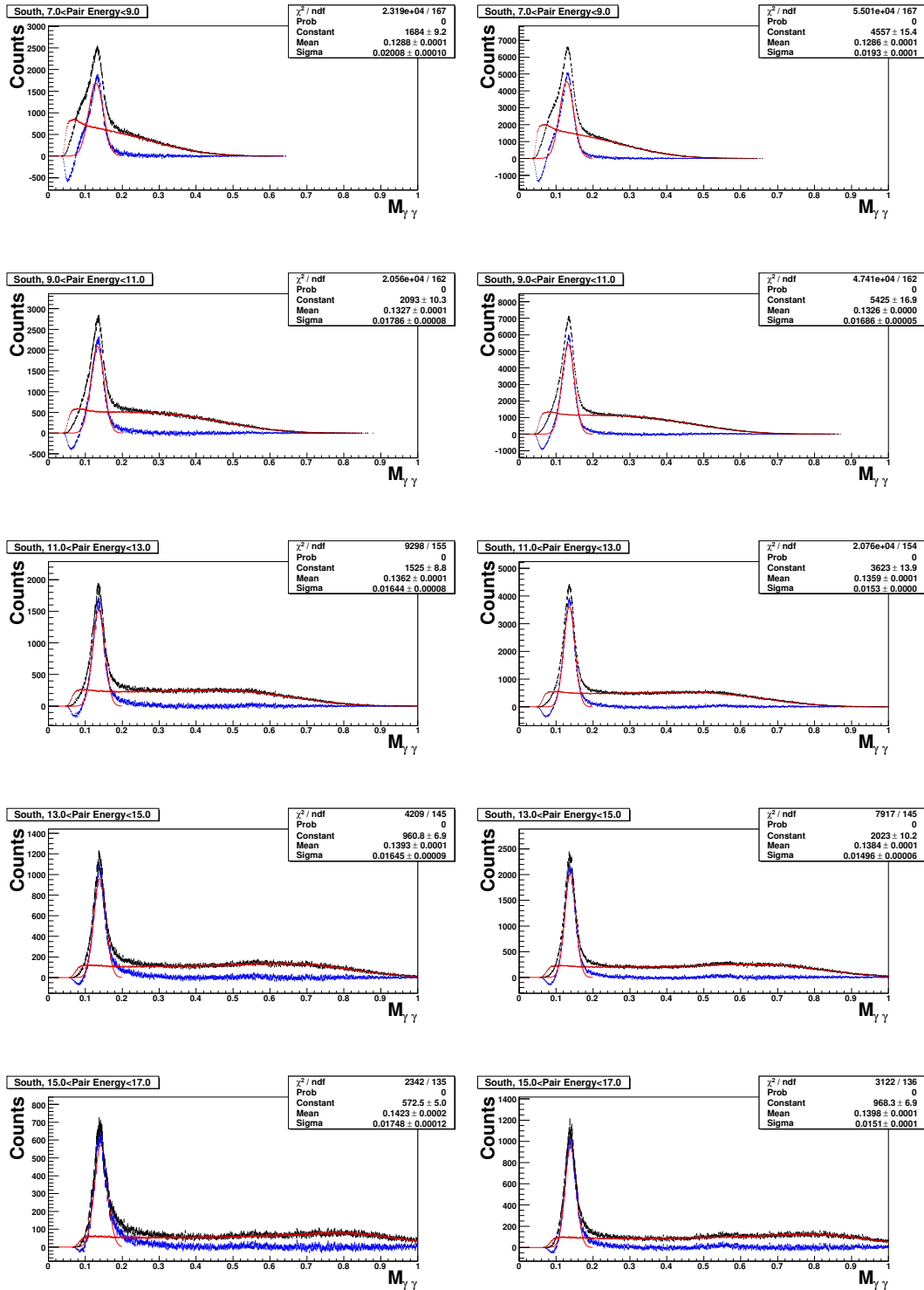


Figure 45: $M_{\gamma\gamma}$ distributions for MPC (left) and Minimum bias (right) triggered data for the South arm in bins of energy

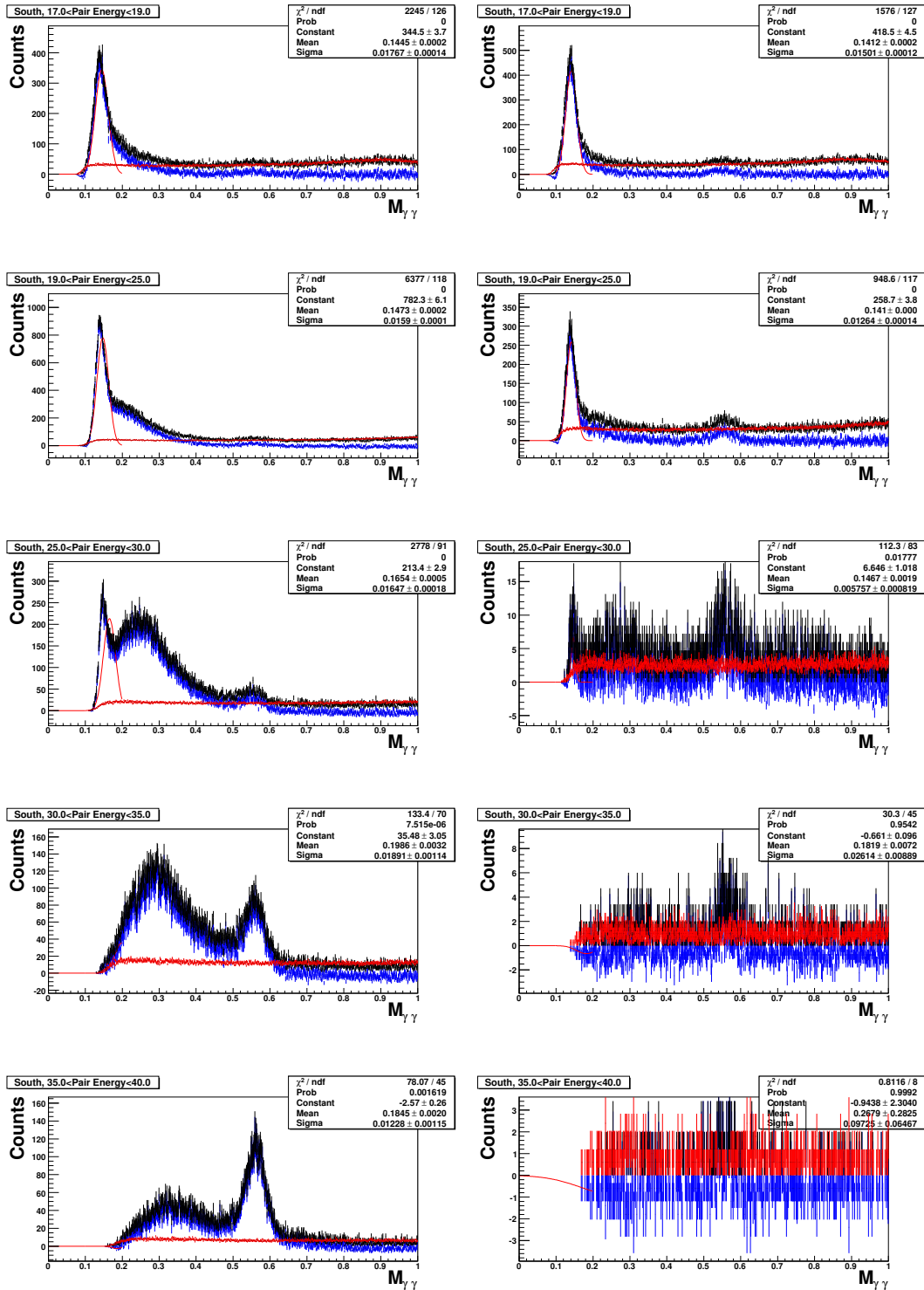


Figure 46: $M_{\gamma\gamma}$ distributions for MPC (left) and Minimum bias (right) triggered data for the South arm in bins of energy

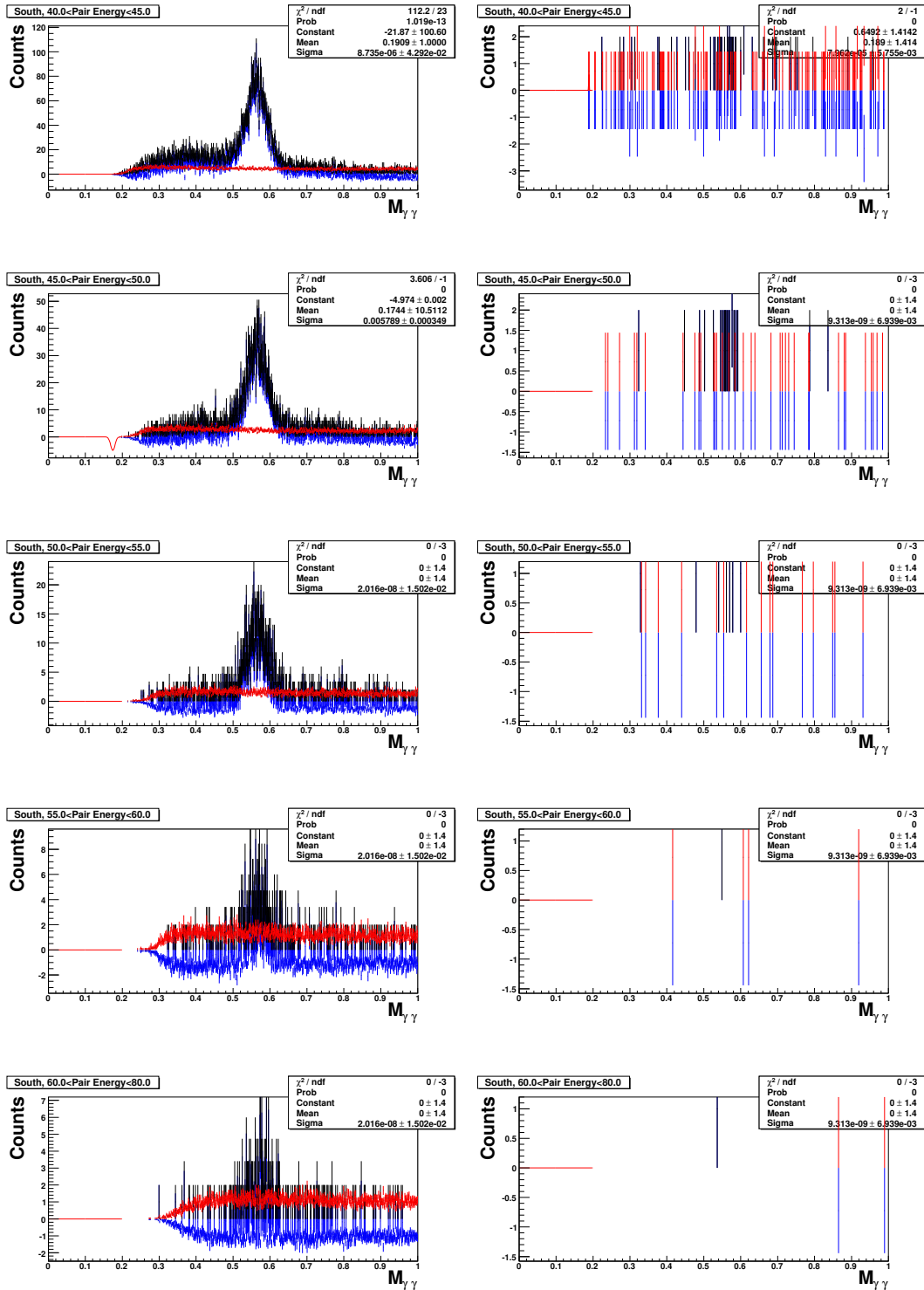


Figure 47: $M_{\gamma\gamma}$ distributions for MPC (left) and Minimum bias (right) triggered data for the South arm in bins of energy

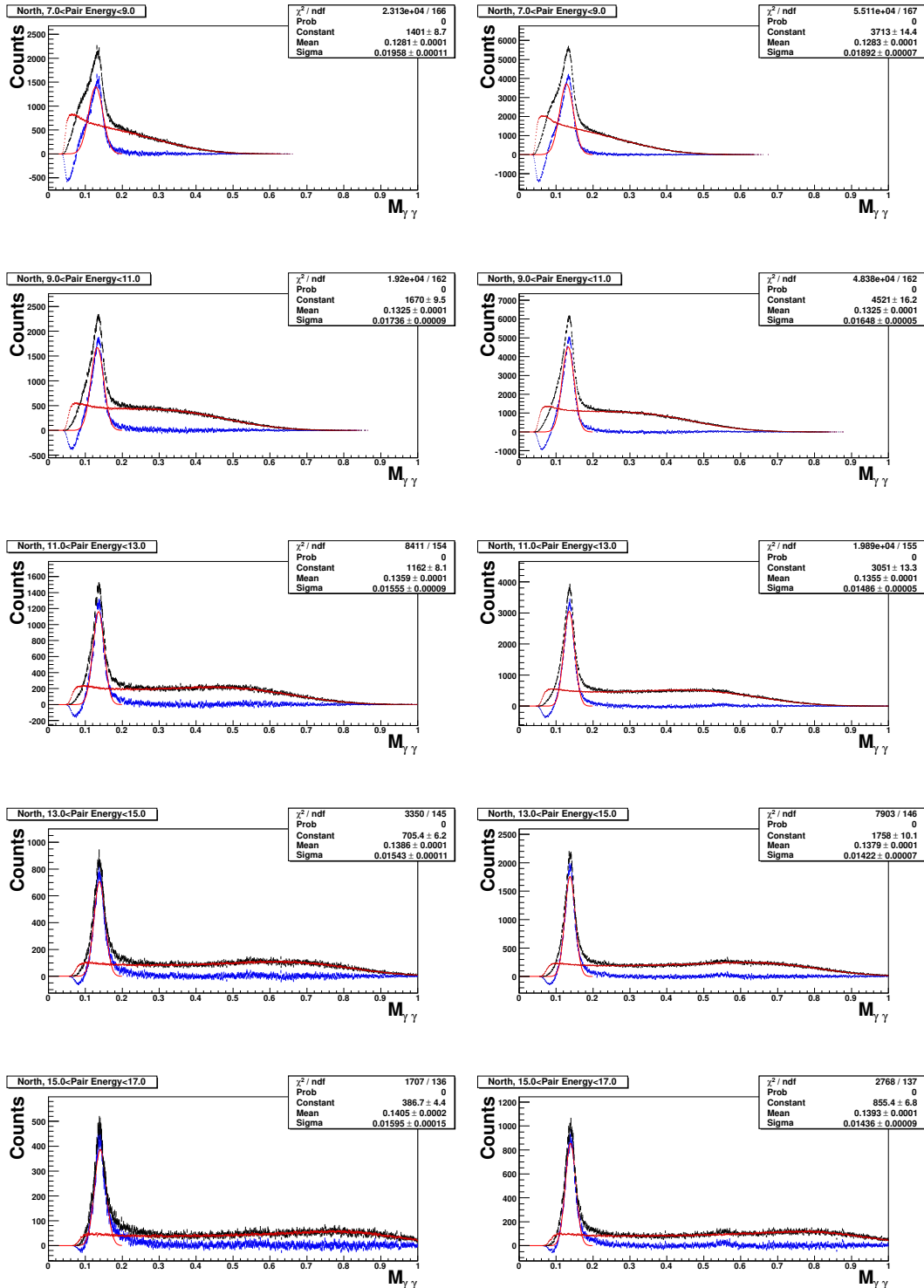


Figure 48: $M_{\gamma\gamma}$ distributions for MPC (left) and Minimum bias (right) triggered data for the North arm in bins of energy

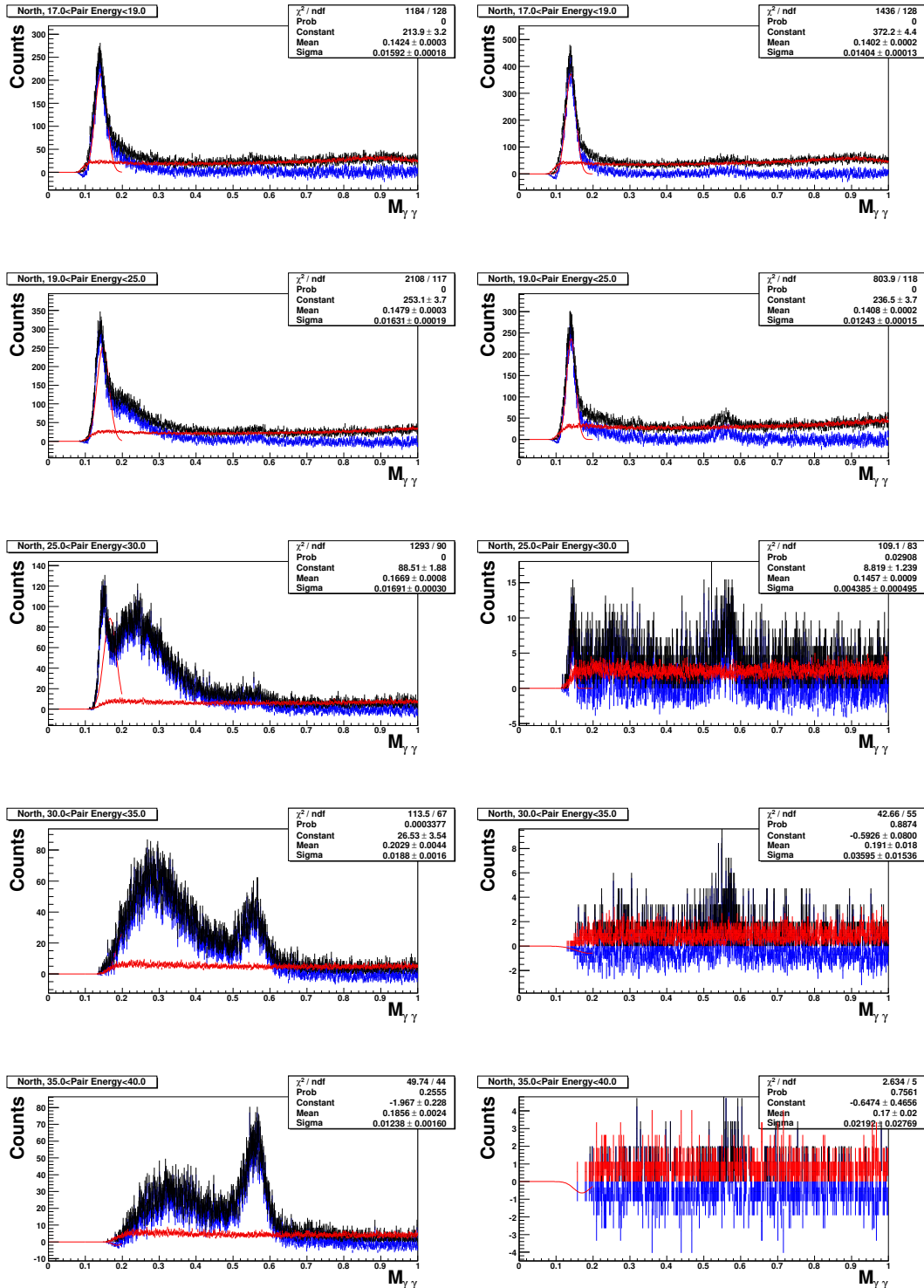


Figure 49: $M_{\gamma\gamma}$ distributions for MPC (left) and Minimum bias (right) triggered data for the North arm in bins of energy

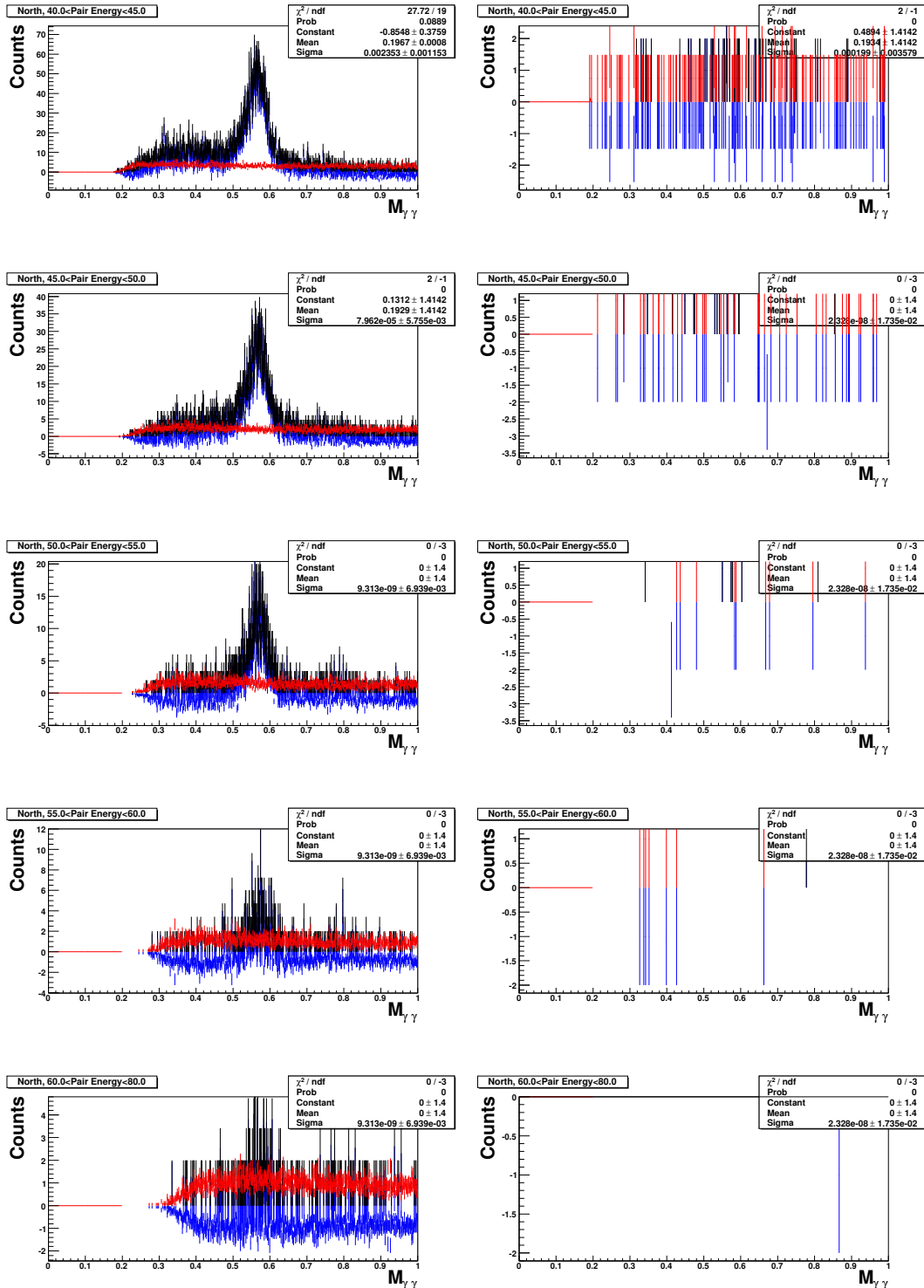


Figure 50: $M_{\gamma\gamma}$ distributions for MPC (left) and Minimum bias (right) triggered data for the North arm in bins of energy

E $M_{\gamma\gamma}$ distributions binned in $p_{T,pair}$ with π^0 fit

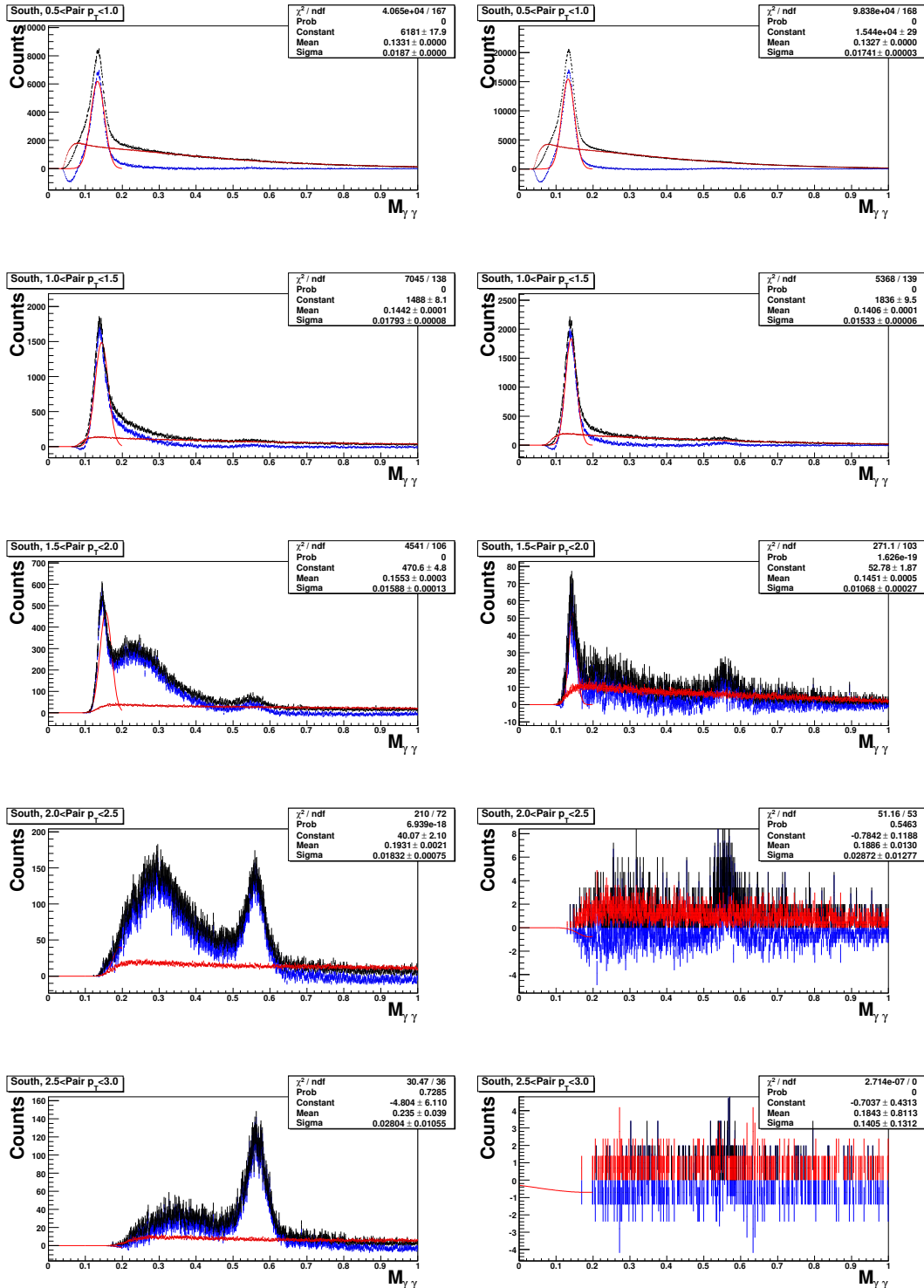


Figure 51: $M_{\gamma\gamma}$ distributions for MPC (left) and Minimum bias (right) triggered data for the South arm in bins of p_T

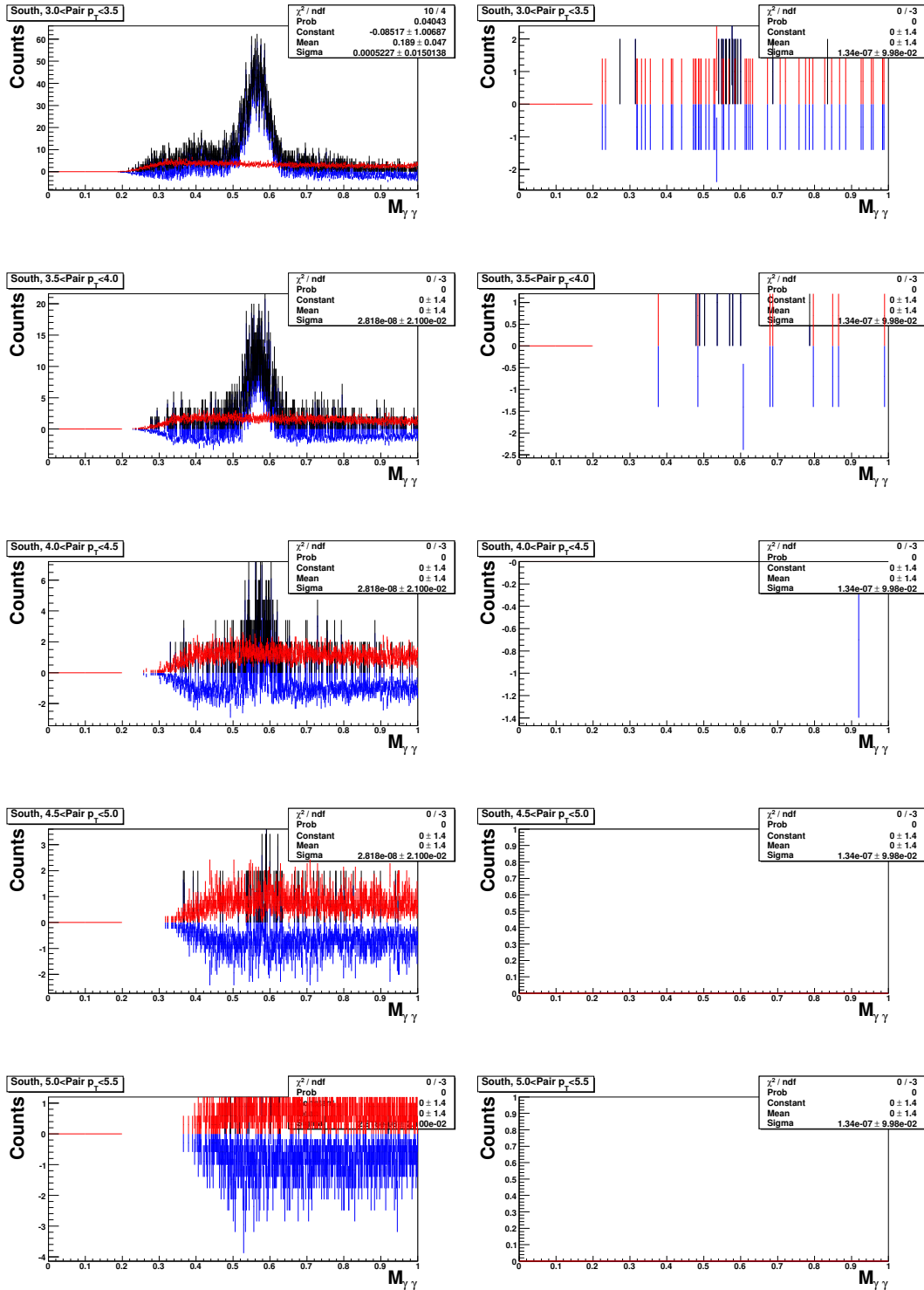


Figure 52: $M_{\gamma\gamma}$ distributions for MPC (left) and Minimum bias (right) triggered data for the South arm in bins of p_T

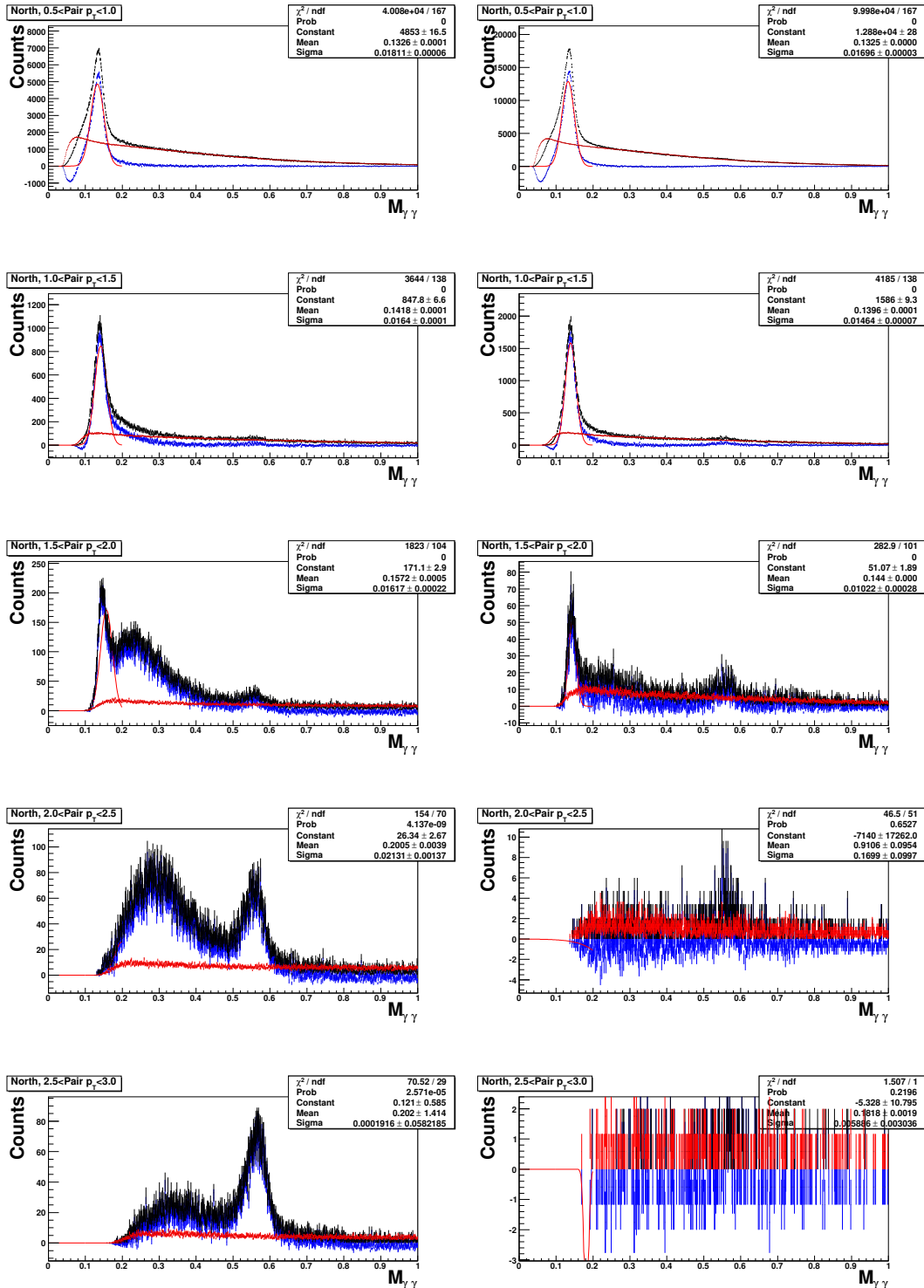


Figure 53: $M_{\gamma\gamma}$ distributions for MPC (left) and Minimum bias (right) triggered data for the North arm in bins of p_T

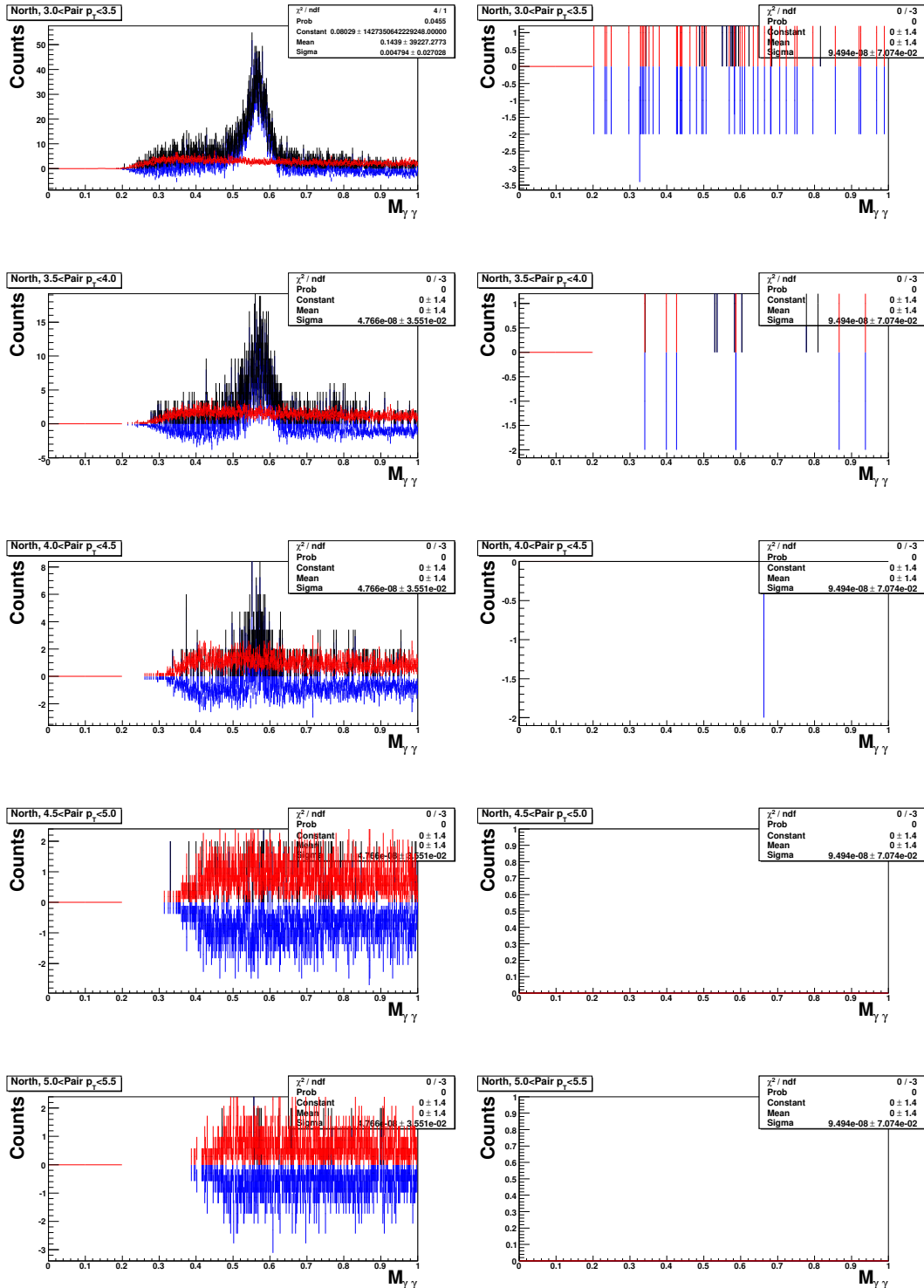


Figure 54: $M_{\gamma\gamma}$ distributions for MPC (left) and Minimum bias (right) triggered data for the North arm in bins of p_T